Modulating Thermal Transport in Polymers and Interfaces: Theories, Simulations, and Experiments

Bo Zhang[1], Peng Mao[1], Yunmin Liang[1], Yan He[2], Wei Liu[1*] and Zhichun Liu[1*]

Bulk polymers are often regarded as thermal insulators due to low thermal conductivity, which extremely limits their applications in the field of heat transfer. Over the past decades, thermal transport in polymers, and polymer nanocomposites has been intensively studied on both theoretical and experimental levels. In addition, novel thermal transport phenomenon involving divergent thermal conductivity in individual polymer chains, giant thermal rectification, has been observed. In this review, the mechanism behind thermal transport in materials, interfacial thermal transport, thermal rectification in polymers, and enhancing thermal transport of polymers are firstly addressed. Secondly, the computational methods for investigating the thermal property of materials mainly focused on molecular dynamics (MD) simulation are summarized and compared. The advanced spectral decomposition methods in non-equilibrium molecular dynamics (NEMD) simulation are highlighted. Thirdly, experimental advances relevant to thermal transport of polymers are briefly reviewed. Finally, the challenges and outlook about modulating thermal transport in polymers and polymer nanocomposites are pinpointed.

1. Introduction

Polymers have been ubiquitously used in industry and daily life owing to various advantages, including chemical inertness, light density, easy of processing, and low cost. As shown in Fig. 1, the thermal conductivity of bulk polymers is often in the range of 0.1~0.5 $Wm^{-1}K^{-1}$, which hinders their applications in thermal management.[1-3] In contrast, Henry and Chen observed divergent thermal conductivity of individual polymer chains in molecular dynamics simulations.[4,5] Experimentally, polymer nanofibres with excellent thermal and mechanical properties have been fabricated.[6-8]

As shown in Fig. 2(a), heat can spontaneously flows from high temperature zone to low temperature zone due to temperature difference. At the macroscale, heat conduction can be described by Fourier's law

$$J = - \kappa \cdot \nabla T \tag{1.1}$$

where J is heat flux, κ is thermal conductivity, and ∇T is temperature gradient. Fourier's law can also be written as

$$Q = - G \cdot \Delta T \tag{1.2}$$

where Q is heat current, G is thermal conductance, and ∇T is temperature difference. The relationship between thermal conductivity

and thermal conductance of the homogeneous material can be given by

$$G = \kappa \cdot A/L \tag{1.3}$$

where A is the cross-sectional area and L is the length of the system. In solid materials, electrons and phonons both contribute to thermal conduction.[9] The total thermal conductivity of non-magnetic materials can be given by

$$\kappa = \kappa_e + \kappa_{ph} \tag{1.4}$$

where κ_e represents the electronic thermal conductivity, and κ_{ph} represents the phononic thermal conductivity. In dielectric material like polymers, the contribution from electrons is negligible and lattice vibration contributes most to the thermal conductivity. Hence phonons, the quanta of lattice vibration modes, are the main heat carriers in dielectric system. Based on kinetic theory, the phononic thermal conductivity can be roughly estimated by Debye equation[10,11]

$$\kappa_{ph} = \frac{1}{3} C_v \overline{v}_g \Lambda \tag{1.5}$$

where C_v is the volumetric specific heat, $\overline{v}_g$ is the average phonon group velocity, and Λ is the phonon mean free path.

As shown in Fig. 2(b), the structure disorder and various defects in bulk polymers extremely reduce the thermal conductivity. Align the

[1]*School of Energy and Power Engineering, Huazhong University of Science and Technology (HUST), Wuhan 430074, China*
[2]*College of Electromechanical Engineering, Qingdao University of Science & Technology, Qingdao 266061, China*
*E-mail: zcliu@hust.edu.cn; w_liu@hust.edu.cn
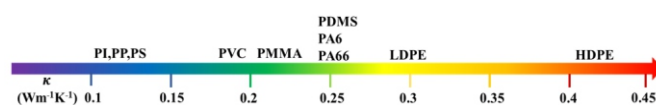
Fig. 1 Thermal conductivities of bulk polymers at room temperature.

orientation of polymer chains can effectively enhance the intrinsic thermal conductivity of polymers.[12] However, in order to tune the chains' orientation, the giant drawing ratio is often necessary.[6] Incorporating high thermal conductive fillers like graphene,[13] carbon nanotube,[14] boron nitride[15] in polymers is another way to elevate the thermal conductivity of polymers. Whereas the thermal conductivity of polymer composites is not as high as expected due to the large interfacial thermal resistance (ITR) between matrix and fillers. Hence declining ITR is critical to enhancing the thermal conductivity of polymer composites. Understanding the thermal transport mechanism in polymers, fillers, across the interface will be helpful to design high thermal conductive materials. Apart from dissipating heat, actively manipulating heat flow is also desired in thermal management.[16] In the past decades, thermal rectification has been extensively studied on the theoretical level while only a few papers report the thermal rectification about polymers.[17] This paper will recount the origin of thermal rectification and summarize recent developments.

In this article, we will first recount the theory about thermal transport, thermal rectification, followed by a brief discussion about the underlying mechanism in modulating thermal transport of polymers. In Sec. 3, state-of-the-art computational methods and spectral decomposition methodology based on NEMD are summarized. In Sec. 4, advanced experimental methods about fabricating high thermal conductive polymers are reviewed. In Sec. 5, the remarks and outlook are given to pinpoint the limitations and directions in theories, simulations, and experiments.

2. Thermal transport theories

2.1 Thermal transport in crystalline materials

In dielectric medium, phonons play a dominant role in heat conduction, whose occupation obeys Bose-Einstein statistics. The thermal conductivity is related to the phonon energy $\hbar\omega(q, j)$, phonon group velocity $v_g(q, j)$, phonon occupation function $f_{BE}(q, j)$, phonon relaxation time[19-21] $\tau(q, j)$

$$\kappa = \frac{1}{V}\sum_{q,j}\hbar\omega(q,j)\frac{\partial f_{BE}(q,j)}{\partial T}v_g(q,j)v_g(q,j)\tau(q,j) \quad (2.1)$$

where V is the volume of the system, q and j denote the phonon wave vector and phonon polarization, respectively. The volumetric phonon specific heat and phonon mean free path can be written as

$$C_v(q,j) = \frac{1}{V}\hbar\omega(q,j)\frac{\partial f_{BE}(q,j)}{\partial T} \quad (2.2)$$

$$\Lambda(q,j) = v_g(q,j)\tau(q,j) \quad (2.3)$$

Substituting Eq. (2.2), (2.3) into Eq.(2.1), we can find that

$$\kappa = \sum_{q,j}C_v(q,j)v_g(q,j)\Lambda(q,j) \quad (2.4)$$

Hence thermal conductivity can be determined by volumetric phonon specific heat, phonon group velocity, and phonon mean free path. Phonon group velocity is defined by

$$v_g(q,j) = \frac{\partial\omega(q,j)}{\partial q} \quad (2.5)$$

Hence phonon dispersion relation is necessary to get phonon group velocity, which is determined by the following secular equation
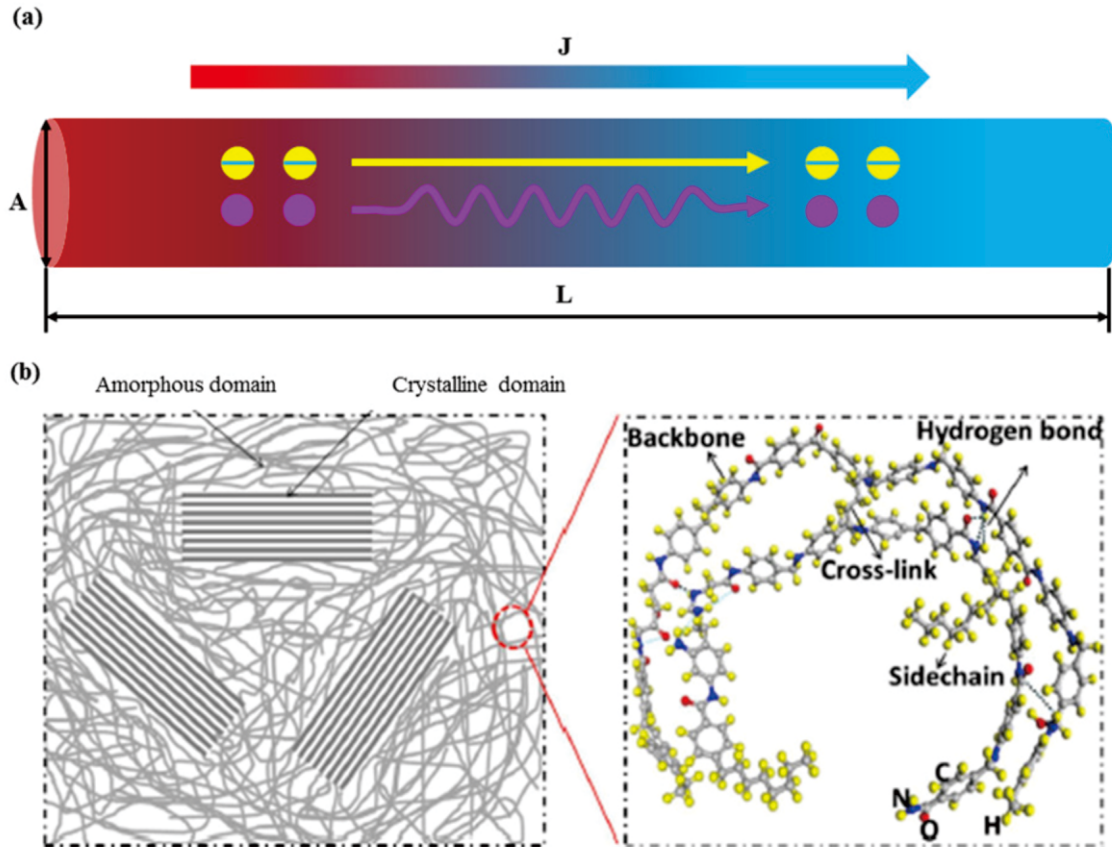
Fig. 2 Schematic illustration of heat conduction and a polymer. (a) Heat conduction in a homogeneous cylinder. (b) The morphology and structure of a polymer.[18] Copyright 2018 Elsevier Ltd.

$$\det ||D_{\alpha\beta}(\boldsymbol{q}) - \omega^2 \delta_{\alpha\beta}|| = 0 \qquad (2.6)$$

where $\alpha, \beta = 1, 2, 3$ represent x, y, z, respectively. D(q) is the 3n × 3n dynamical matrix (n is the number of atoms per unit cell.). The elements of the dynamical matrix are

$$D_{\alpha\beta}(ss',\boldsymbol{q}) = \frac{1}{\sqrt{M_s M_{s'}}} \sum_l \Phi_{\alpha\beta}(l,ss') e^{(i\boldsymbol{q}\cdot[r(s',l) - r(s,0)])} \qquad (2.7)$$

where s and s′ denote an atom in the *l*-th unit cell, *l* = 0 refers to the reference unit cell, M and **r** denote the mass and position of the atom. In order to accurately determine phonon dispersion, accurate empirical potential function or first principle calculation is essential. In addition, the size of the system cannot be too large due to the time consuming calculation. Fig. 3 displays some common atomic structures and the corresponding phonon dispersion relation. It can be seen that all the phonon frequency of the system is positive. More phonon branches will emerge with the increasing number of atoms in the primitive cell. Compared with low frequency phonons, the group velocity of high frequency phonons is much smaller. This confirms that low frequency phonons often play an important role in heat conduction.

Based on Eq. (2.1)~(2.4), another crucial factor affecting thermal conductivity is phonon relaxation time, which is intensively related to phonon interaction in the material. In pure dielectric crystal, phonon-phonon scattering induced by anharmonic interaction becomes the main source of scattering. The extremely high thermal conductivity of carbon nanotube[22] (CNT) and graphene[23-25] is attributed to the strong atomic bonding and low anharmonicity. For low frequency phonons, the phonon mean free path in CNT and graphene can reach the order of microns. Compared with CNT and graphene, the high thermal conductivity of boron arsenide (BAs) is mainly due to the large phonon band gap and relatively weak phonon-isotope scattering.[26-29] The large

band gap and conservative conditions can effectively increase the phonon relaxation time.

As shown in Fig. 4, in realistic dielectric materials, more phonon scattering channels will emerge owing to various defects like vacancy, impurity, electron, dislocation, grain boundary, external perturbation, *et al.*[33,34] According to Matthiessen's rule, the total phonon scattering rates are equal to the summation of phonon scattering rates in individual process,

$$\frac{1}{\tau} = \frac{1}{\tau_{Ph-i}} + \frac{1}{\tau_{Ph-e}} + \frac{1}{\tau_{Ph-b}} + \frac{1}{\tau_{Ph-Ph}} + \dots \qquad (2.8)$$

where $\frac{1}{\tau}$, $\frac{1}{\tau_{Ph-i}}$, $\frac{1}{\tau_{Ph-e}}$, $\frac{1}{\tau_{Ph-b}}$ and $\frac{1}{\tau_{Ph-Ph}}$ denote the total phonon scatterings, phonon-impurity scatterings, phonon-electron scatterings, phonon-boundary scatterings, and phonon-phonon scatterings, respectively. However, Matthiessen's rule may overestimate the thermal conductivity owing to the neglect of the coupling among different scattering process.[35] Meanwhile, accurately calculating phonon scattering rates in individual process like electron-phonon scattering is not trivial and a better understanding of phonon scatterings will be useful to modulate the thermal conductivity of materials.

2.2 Thermal transport in amorphous materials

In contrast with crystal, lacking translational symmetry is the most distinguishable feature of amorphous dielectric material. Hence phonons are only used to denote the energy quanta of lattice vibration for amorphous materials. Phonon wave vector and group velocity are not well defined for the majority of states. For amorphous polymers, thermal transport more likely depends on the phonon hopping process.[36] Feldman and Allen *et al* propose to use "propagons, diffusons, and locons" to replace the phonons.[37-40] The total thermal conductivity can be written as

$$\kappa = \kappa_{pr} + \kappa_{dif} + \kappa_{lo} \qquad (2.9)$$
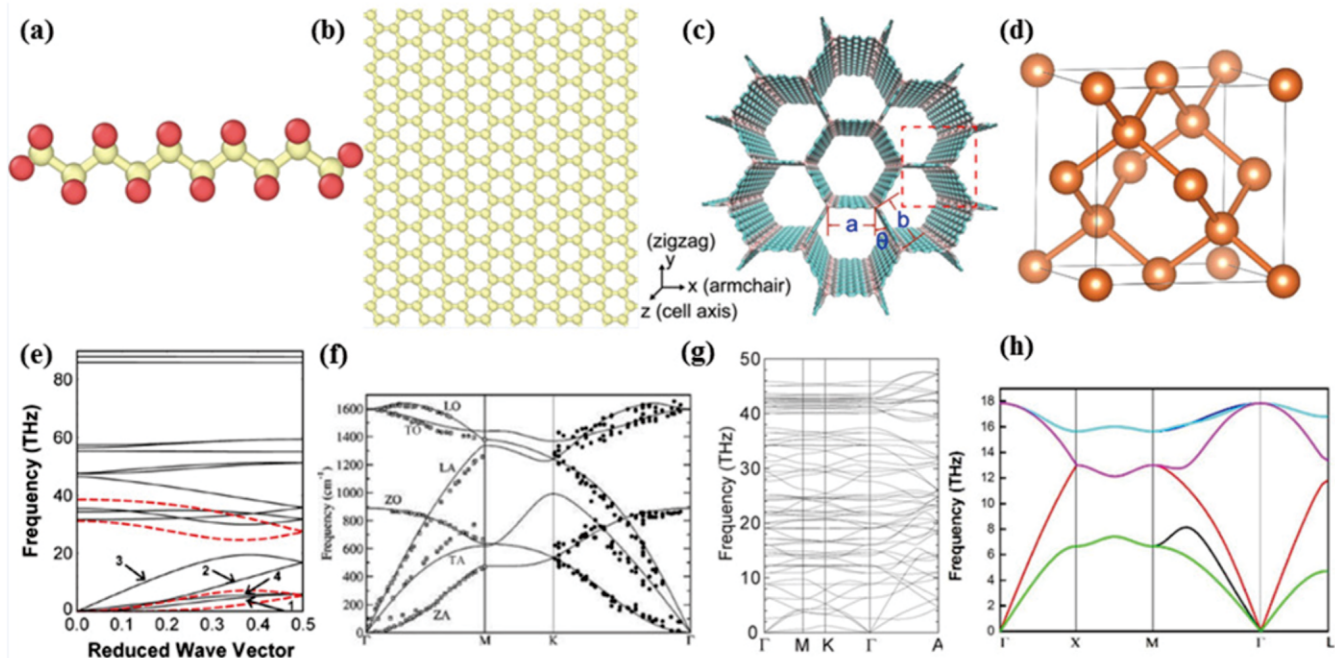
Fig. 3 Schematic of atomistic structure and corresponding phonon dispersion. (a) Single PE chain. (b) Graphene sheet. (c) C-honeycomb structure.[30] Copyright 2016 American Chemical Society. (d) Silicon. (e) Phonon dispersion of the single PE chain. Copyright 2008 American Physical Society. (f) Phonon dispersion of the graphene sheet.[31] Copyright 2003 American Physical Society. (g) Phonon dispersion of the C-honeycomb.[30] Copyright 2016 American Chemical Society. (h) Phonon dispersion of the silicon.[32] Reproduced figure h with permission.

where κ_{pr}, κ_{dif}, and κ_{lo} are the contribution from propagons, diffusons, and locons, respectively. As shown in Fig. 5, propagons and diffusons are extended modes, while locons are localized modes.

$$\kappa_{pr} = \sum_{\boldsymbol{q},j}^{\omega < \omega_{IR}} C_v(\boldsymbol{q},j)\, v_g(\boldsymbol{q},j) \Lambda(\boldsymbol{q},j) \qquad (2.10)$$

where ω_{IR} is the cutoff frequency of the propagons. In contrast, diffusons and locons don't have well-defined group velocity, whose contribution to thermal conductivity can be described by

$$\kappa_{dif} + \kappa_{lo} = \sum_{\omega_{IR} < \omega < \omega_{max}} C_v(\omega)\, D_i(\omega) \qquad (2.11)$$

$$D_i = \frac{\pi V^2}{3\hbar^2 \omega_i^2} \sum_{j \neq i} \left| S_{ij} \right|^2 \delta(\omega_i - \omega_j) \qquad (2.12)$$

where ω_{max} is the maximum frequency of density of states, D_i is the mode diffusivity, $S_{ij} = <i|S|j>$ is the intermode matrix element of the heat current operator, and δ is the Dirac delta function. The heat current operator denotes the interaction of vibrational modes, which is related to the spatial overlap and spring constants.[41] Propagons and diffusons can be distinguished by specifying Ioffe-Regel limit.[42] Larkin and McGaugyhey *et al* propose to use structure factors to distinguish propagons and diffusons. The structure factor is defined as

$$S^{L,T}(\boldsymbol{q},\omega) = \sum_j E^{L,T}(\boldsymbol{q},j)\, \delta(\omega - \omega(\boldsymbol{q},0)) \qquad (2.13)$$

where the summation is over the gamma modes, E^L and E^T refer to the longitudinal and transverse polarization, respectively.[43] However, this method requests that the mode character must change abruptly in the vicinity of Ioffe-Regel crossover. In order to distinguish the propagons and diffusons, Lv and Henry *et al* recommend measuring the eigenvector periodicity (EP) for each mode.[44,45] The normalized EP can be given by

$$\gamma_n = \frac{\left| \sum_s \sum_{s' \geq s} [\boldsymbol{e}_{s,n} \cdot \boldsymbol{e}_{s',n}][f(\boldsymbol{q}' \cdot \boldsymbol{r}_s + \varphi')f(\boldsymbol{q}' \cdot \boldsymbol{r}_{s'} + \varphi')] \right|}{\left| \sum_s \sum_{s' \geq s} [\boldsymbol{e}'_{s,n} \cdot \boldsymbol{e}'_{s',n}][f(\boldsymbol{q}' \cdot \boldsymbol{r}_{s0} + \varphi')f(\boldsymbol{q}' \cdot \boldsymbol{r}_{s'0} + \varphi')] \right|} \qquad (2.14)$$

where $\boldsymbol{e}$, $\boldsymbol{e}'$, refer to the eigenvector of the real mode and fictitious periodic mode, n is the mode index; $\boldsymbol{q}'$, φ' refer to the wave vector and phase of the fictitious mode, respectively. The large value of γ_n denotes the mode is propagating, while the small value of γ_n denotes the mode is
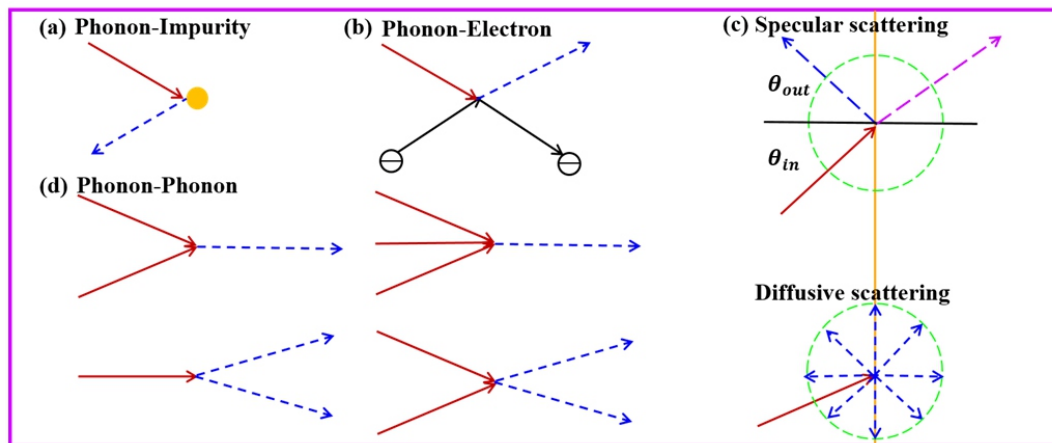
Fig. 4 Schematic illustration of various phonon scatterings. (a) Phonon-impurity scattering. (b) Phonon-electron scattering. (c) Phonon-boundary scattering. (d) Phonon-Phonon scattering.
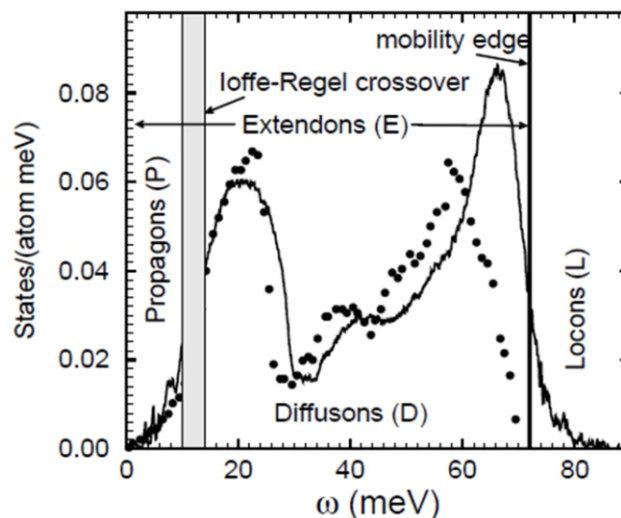
Fig. 5 Phonon density of states (DOS) of amorphous silicon.[39] Copyright 1993 American Physical Society.
Note: the x-axis unit here is the energy unit ($\hbar\omega$)

non-propagating.

Locons are localized modes whose eigenvector decays dramatically with distance from the center. The participation ratio[46] (PR) can be used to distinguish extended modes (propagons, diffusons) and localized modes, which is given by

$$PR_n = \frac{(\Sigma_s e_{s,n}^2)^2}{N \Sigma_s e_{s,n}^4} \qquad (2.15)$$

The PR characterizes the proportion of atoms participating in an eigenvibration, whose numerical range is 0~1. With respect to harmonic system, all the atoms participate in eigenvibration and thus PR is 1. For real system with impurities, boundaries and interfaces, only a part of atoms participate in eigenvibration and thus PR will decrease. Accurate eigenvector may be not accessible for large size super cell due to limited computational resource. Without considering phonon polarization, the mode PR[47,48] can be given by

$$PR(\omega) = \frac{1}{N} \frac{(\Sigma_s DOS_s(\omega)^2)^2}{\Sigma_s DOS_s(\omega)^4} \qquad (2.16)$$

where N is the number of atoms in the system, $DOS_s(\omega)$ is the local DOS of s-th atom calculated from Fourier transformation of normalized velocity autocorrelation function (VACF)[49]

$$DOS(\omega) = \int_{-\infty}^{+\infty} \frac{<v(0) \cdot v(t)>}{<v(0) \cdot v(0)>} \cos(\omega t) dt \qquad (2.17)$$

where v is the atomic vibrational velocity. Compared with extended modes, the localized modes have smaller PR. Extended modes and localized modes play different role in heat conduction with respect to different materials. Fig. 6 displays the structure image, corresponding PR spectra and DOS of silicon phononic crystals (Si-PnCs), amorphous silicon (a-Si), amorphous silica (a-SiO$_2$), and atactic PS. As shown in Fig. 6(a) and (e), phonons are localized in the vicinity of spherical hole and have low participation ratio.[50] The DOS and PR spectra in Fig. 6 (f)-(h) indicate that high frequency phonons are more likely to be localized compared with low frequency phonons. For Si-PnCs and a-Si, localized modes make negligible contribution to the thermal

conductivity. Harmonic theory can be successfully applied to these systems with one type of atom and identical interaction potential. However, for a-SiO$_2$ and atactic PS, localized modes make a moderate contribution to the thermal conductivity through anharmonic coupling. Harmonic theory fails to predict thermal conductivity of these systems with complex composition.[51] In contrast, MD simulation with full anharmonic potentials is suitable for these complex systems.

2.3 Thermal transport across interface

Interfacial thermal transport is crucial to thermal management of microelectronics[52,53] and thermal transport of polymer nanocomposites[54-56] due to high interface density in these systems. As shown in Fig. 7(a), the temperature difference ΔT will emerge at the interface when heat flows through different medias. The interfacial thermal conductance (ITC) G is given by[57-59]

$$G = J/\Delta T \qquad (2.18)$$

where J is the heat flux across the interface. The ITR is the reciprocal of ITC. The acoustic mismatch model[60] (AMM) and diffuse mismatch model[61] (DMM) are two simple models in estimating ITC. However, AMM assumes phonons undergo specular reflection and transmission, which is only reasonable at low temperature. DMM assumes that phonons at the interface undergo diffusive scattering, which suits for the wavelength of phonons much shorter than the surface roughness. The transmissivity of DMM can be given by

$$\mathcal{T}(\omega) = \frac{\Sigma_{j2} DOS_2(\omega) v_{g2}}{\Sigma_{j1} DOS_1(\omega) v_{g1} + \Sigma_{j2} DOS_2(\omega) v_{g2}} \qquad (2.19)$$

It can be seen from Eq. (2.20) that DMM only considers elastic scattering. Hence DMM cannot apply in high temperature condition, where anharmonic effect plays an important role in interfacial thermal transport. Hida and Shiomi discover that ITC of CNT/PE composites increases with the increasing temperature due to the enhanced inelastic thermal transport.[62] Wu and Luo discover that the anharmonicity inside the material can facilitate phonon mode conversion and thus contribute to interfacial thermal transport.[63] Feng *et al* find that the inelastic
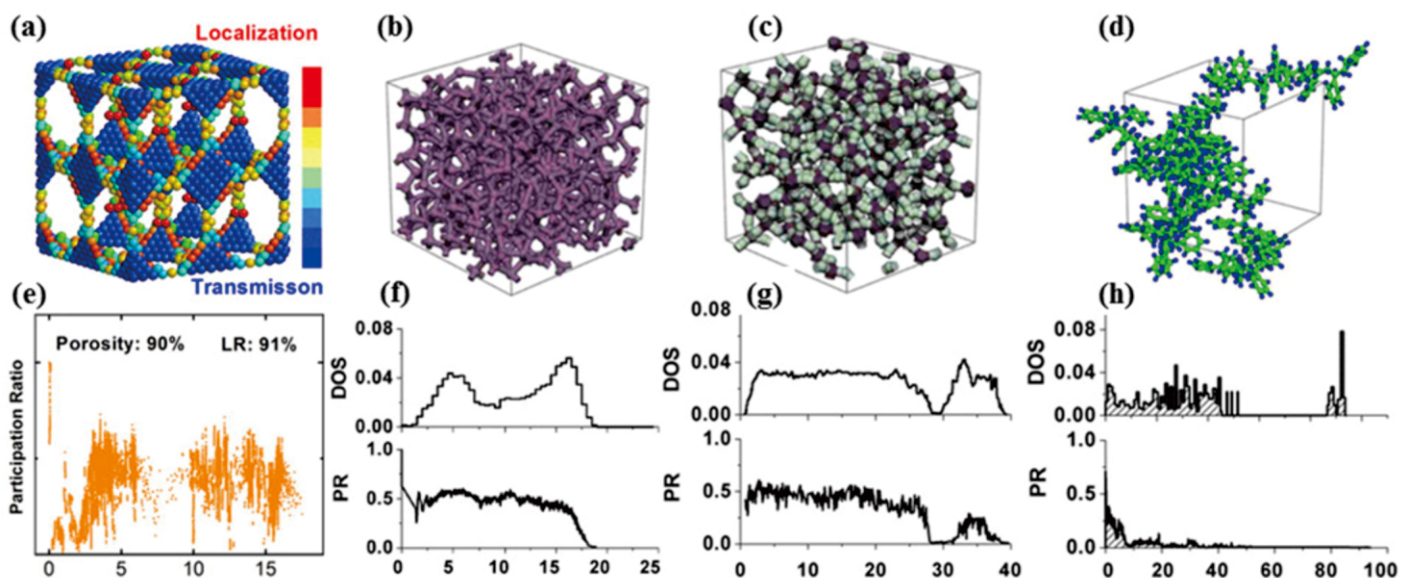
Fig. 6 Structure of four materials with the corresponding participation ratio spectra and DOS. (a) Structure image and normalized energy distribution of the Si PnCs. (b) Structure of a-Si. (c) Structure of a-SiO$_2$. (d) Structure of atactic PS. (e) Participation ratio spectrum of Si-PnCs. Localization ratio refers to localization ratio. Copyright 2014 American Chemical Society. (f) DOS and PR spectra of a-Si. (g) DOS and PR spectra of a-SiO$_2$. (h) DOS and PR spectra of atactic PS. (Ref. [50,51]) Copyright 2009 American Institute of Physics.

transport can contribute more than 50% to the ITC of silicon/germanium (Si/Ge) heterostructure.[64] The anharmonic interaction enables optical phonons to contribute to interfacial thermal transport.[64-66] Different from traditional lattice dynamics method, spectral decomposition method in MD simulation can fully capture the anharmonic effect and deliver deep insight about interfacial thermal transport from frequency level. With respect to thermal transport in polymers, spectral decomposition based on MD has less limits, which will be described in Sec 3.3.

Fig. 7(b) shows the h-BN and graphene heterostructure with different interface. Defects like isotopes,[67-69] vacancies,[70,71] and dislocations[72,73] are often detrimental to thermal transport. Contrary to conventional belief, interfacial defects unexpectedly facilitate thermal transport across the interface. Liu *et al* find that h-BN/graphene interface with topological defects has a higher ITC than the pristine interface due to the local stress field near the pores.[74] Giri and Hopkins *et al* discover that atomic mass defects at the interface can enhance ITC of amorphous SiOC:H/SiC:H interface due to the emergence of interfacial modes.[75] The coupling between interfacial modes and bulk modes facilitates the thermal transport across the interface.

Fig. 7(c) and (d) show that ITC can be enhanced by employing the intermediate layer (IL) to bridge vibrational power spectra (VPS). The VPS is similar to DOS and can be given by[63]

$$\text{VPS}(\omega) = \frac{1}{2} m_s \left| \int_0^\tau < \boldsymbol{v}_s(0) \cdot \boldsymbol{v}_s(t) > e^{-i\omega t} dt \right| \quad (2.20)$$

or[66]

$$\text{VPS}(\omega) = \frac{1}{N} \sum_{s=1}^N \left| \int_0^\tau \sqrt{m_s} \cdot \boldsymbol{v}_s \, e^{-i\omega t} dt \right|^2 \quad (2.21)$$

where m_s is the mass of s-th atom, $\boldsymbol{v}_s$ is the vibrational velocity of s-th atom, ω is the phonon angular frequency. The spectral temperature $T_{sp}(\omega)$ can be defined as

$$T_{sp}(\omega) = \frac{\text{VPS}^{neq}(\omega)}{\text{VPS}^{eq}(\omega)} T^{eq} \quad (2.22)$$

$$S = \frac{\int_0^{\omega cut} VPS_1(\omega) VPS_2(\omega) d\omega}{\sqrt{\int_0^{\omega c \upsilon \ddagger} VPS_1(\omega)^2 d\omega} \sqrt{\int_0^{\omega c \upsilon \ddagger} VPS_2(\omega)^2 d\omega}} \quad (2.23)$$

Clearly, the larger value of S indicates the better match of VPS and more efficient interfacial thermal transport. Luo *et al* discover that ITC between gold (Au) and PE can be increased by 7 folds by employing SAM as IL owing to the better match of VPS between SAM and PE.[78]

Apart from matching degree of VPS, the alternative indexes like interfacial binding energy, the effective contact area, the atomic number density near the interface can be used to evaluate the interfacial thermal transport. The higher interfacial binding energy[79,80] and larger effective contact area[81] can be realized by choosing proper SAM as IL, which can effectively enhance the ITC.

2.4 Thermal rectification of polymers

Thermal rectification (TR) can be used to control the heat current, which has great potential in thermal management[82] and phononic information technology.[83-85] The TR ratio η can be defined as

$$\eta = \frac{J_+ - J_-}{J_-} = \frac{\kappa_+}{\kappa_-} - 1 \quad (2.24)$$

where J_+, J_-, κ_+, κ_- denote forward heat flux, backward heat flux, forward thermal conductivity, and backward thermal conductivity, respectively. The nonlinear interaction is the key in TR, which ensures the phonon mode conversion among different frequencies.[86-88] As shown in Fig. 8(a), the TR can be induced by the mismatch of VPS for dissimilar anharmonic systems, which results from the weak coupling at the interface.[89-92] The asymmetry of geometry,[93-95] mass distribution,[96,97] and defects distribution[98-100] can also induce mismatch of VPS to get high TR ratio in conjunction with nonlinear interactions. However, the TR ratio of CNT deposited $C_9H_{16}Pt$ at room temperature is only 2%.[96] Previous simulations have shown that the considerable TR ratio can be reached in asymmetrical nanostructures like asymmetrical graphene
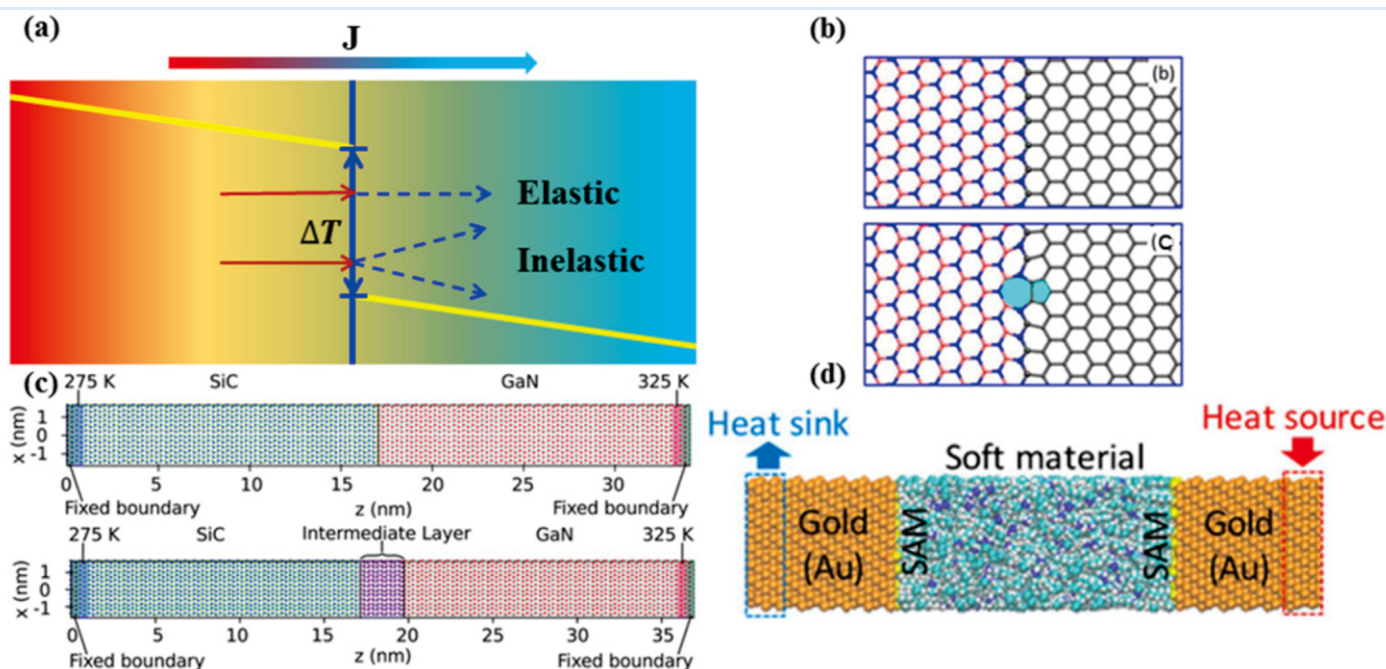
Fig. 7 Schematic of interfacial thermal transport and simulation set up in MD. (a) Schematic illustration of interfacial thermal transport. (b) Heterostructure of h-BN and graphene with coherent interface and incoherent interface with topological defects.[74] Copyright 2016 American Chemical Society. (c) Schematic of SiC/GaN and SiC/IL/GaN structure.[66] Copyright 2017 Royal Society of Chemistry. (d) Schematic of Au-SAM/hexylamine structure.[79] Copyright 2017 American Chemical Society.

nanoribbons[94,95,101] and junctions.[77,102] Nevertheless, the giant temperature difference in such a small system is undesired in applications. The temperature itself has a nonlinear effect on phonons. Phonons are more likely to be nondiffusive transport in small size graphene and CNT, which is difficult to implement in industry due to large size of the material. Recently, a TR factor of 26% has been achieved in a large-area monolayer graphene with nanopores on one side.[100] However, the expensive cost and elaborate manufacturing of graphene with nanopores hinder the application. Compared with graphene, the cost of polymers is so low that they are hopeful for large-scale industrial applications.

Fig. 8(b) shows that the TR can emerge at the dissimilar bimaterial junction, which is related to the phonon localization.[101,103,104] The degree of phonon localization determines the available phonon transport channels, which is intimately related to the thermal transport. Based on phase dependent thermal conductivity, the thermal diode can be constructed by PE with different morphology (Fig. 8(c)). The linear PE will become disordered at high temperature, while the cross-link PE (PEX) still keeps the pristine phase. The reverse temperature bias can change the phase of linear PE and thus result in TR.[105] Moreover, Tian *et al* discover that the phonon transport mechanism will change when the direction of heat flow reverses.[106] The underlying mechanism is related to the structural transition and phonon transmission between side chains and the backbone.

2.5 Enhancing intrinsic thermal transport and interfacial thermal transport
Enhancing thermal conductivity of polymers can greatly expand their application in heat transfer. For crystalline polymers, thermal transport can be well described with the help of phonon picture. For noncrystalline polymers, thermal transport mechanism still needs to be investigated. As shown in Fig. 9(a), high crystallinity,[8] good chain orientation,[6,14,107] ordered morphology,[108] less side chains,[109] stiff and extended polymer backbone,[110,111] confined angular bending,[112] efficient thermal conductive pathways[113,114] are beneficial to thermal transport of polymers. The underlying mechanism is that they can increase phonon group velocity or phonon relaxation time.

Interfacial thermal transport is essential for improving the thermal conductivity of polymer nanocomposites due to large specific surface area. With respect to thermal transport across the interface, not only thermal transport inside polymers and fillers but also interfacial atomic interaction is worthwhile to consider. As shown in Fig. 9(b), similar atomic vibration near the interface,[79] high interfacial binding energy,[115] large contact area,[81] strong filler-matrix coupling[116] can lead to efficient interfacial thermal transport. The reason is that they can provide more channels for phonons to transmit through the interface. Hence in order to enhance the thermal conductivity of polymers, not only high thermal conductive fillers but also proper polymer matrix is necessary to select.

3. Computational methods and their applications in polymers
3.1 Comparison of micro/nanoscale computational methods
Detailed depiction of simulation methods at micro/nanoscale has been reviewed from different perspectives.[48,117,118] Table 1 summarizes the
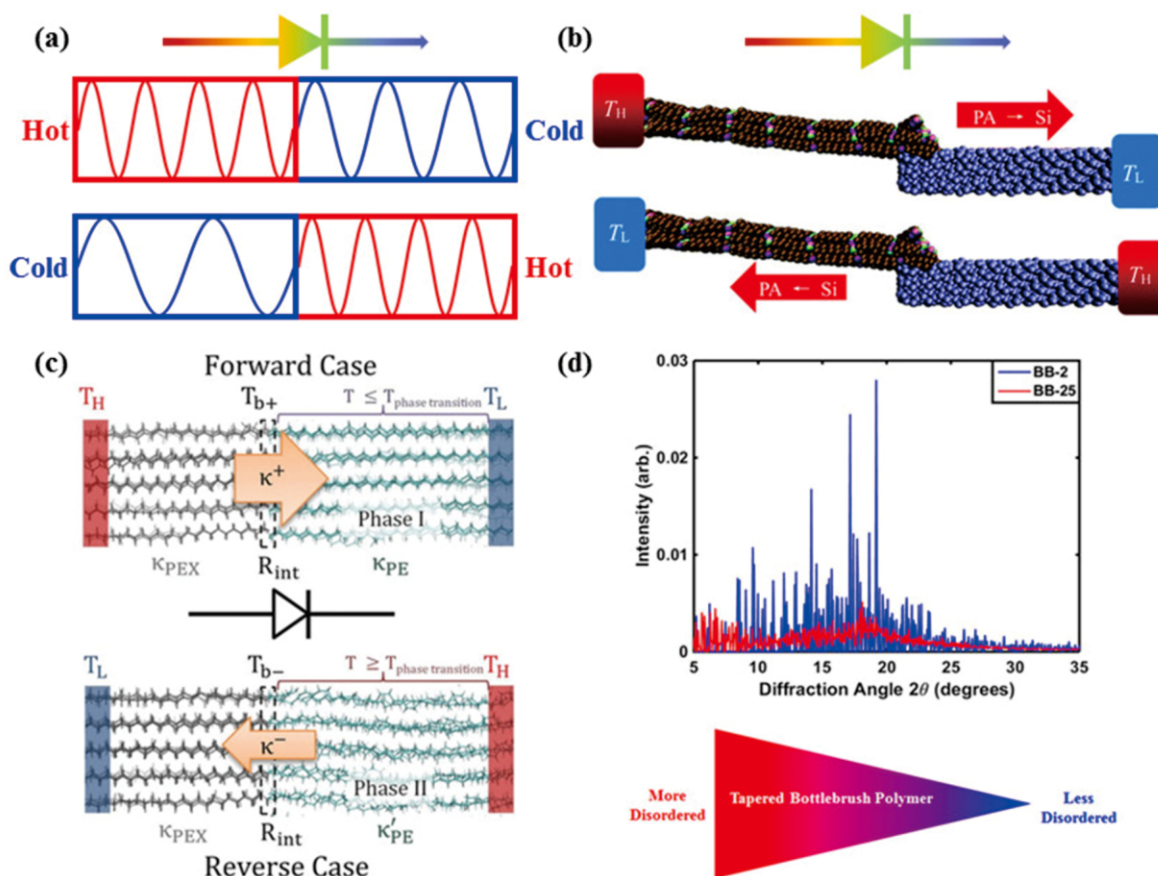

Fig. 8 (a) Schematic illustration of thermal rectification.[92] (b) Schematic of PA/Si junction.[103] Copyright 2017 Royal Society of Chemistry. (c) Schematic of PE/PEX junction.[105] Copyright 2014 John Wiley and Sons. (d) Schematic of bottlebrush polymer and the XRD pattern.[106] Copyright 2017 American Chemical Society.

features about the popular simulation methods involving Boltzmann transport equation (BTE), MD simulation, and atomistic Green's function (AGF). Compared with BTE and AGF, MD is more suitable to investigate thermal transport of polymers due to many atoms in the supercell.

## 3.2 Fundamentals about molecular dynamics simulation

Although MD is a powerful tool to investigate thermal transport of polymers at the molecular level, the assumptions and limitations are worthwhile to be noted. One assumption is the Born-Oppenheimer approximation, which separates the motion of atomic nuclei and electrons. Theoretically, the atomic motion needs to be described by Schrodinger equation. However, solving Schrodinger equation is time consuming and computational expensive. One critical approximation is to assume the atomic motion obeys classical Newton's second law[120]

$$m_i \frac{d^2 r_i}{dt^2} = F_i = -\frac{\partial U_i}{\partial r_i} \tag{3.1}$$

Table 1 Comparison of popular simulation methods at micro/nanoscale.

Simulation methods	Features	Shortcomings	Application range
Boltzmann transport equation [48]	(1) Phonons obey quantum distribution (2) Couple with first principle calculation	(1) Ignore wave effect (2) Successive phonon scatterings are independent [5]	crystalline material with weak anharmonicity
Molecular dynamics simulation [118]	(1) Permit simulating large super cell (2) Involve all order anharmonicity of lattice vibration	(1) Ignore quantum effect (2) Depend on the accuracy of potential energy function	System at moderately high temperature
Atomistic Green's function [119]	(1) Involve phonon wave effect (2) Phonons obey quantum distribution	Ignore phonon anharmonicity	System at low temperature
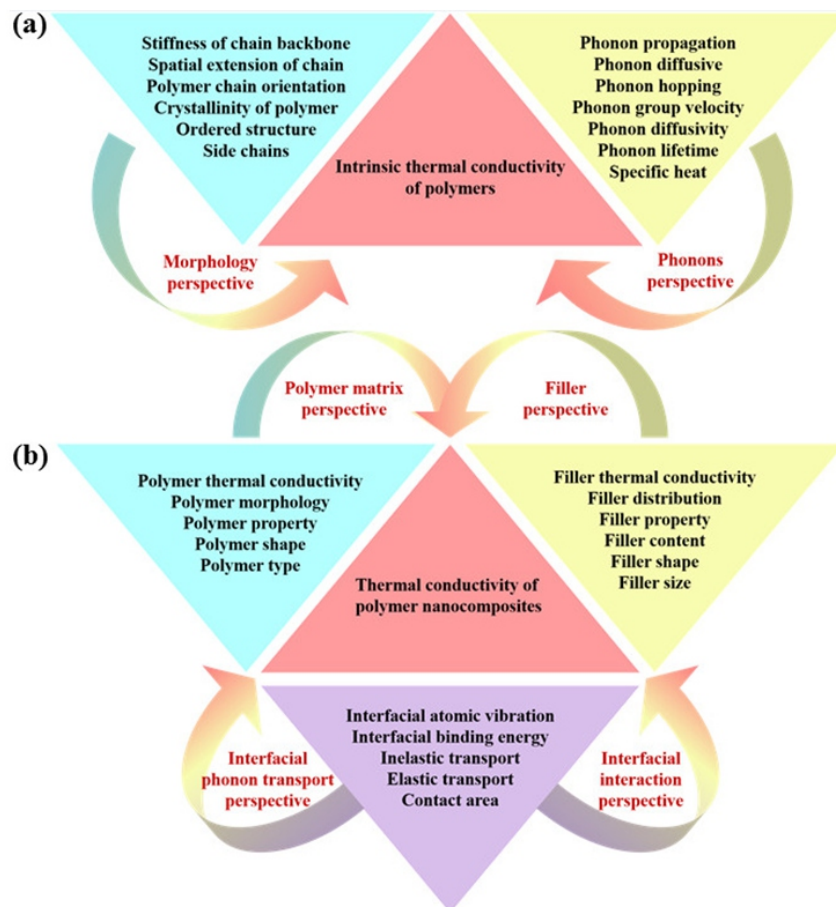
Fig. 9 Crucial factors affecting the thermal conductivity of polymers and polymer nanocomposites. (a) Crucial factors affecting the intrinsic thermal conductivity of polymers. (b) Crucial factors affecting the thermal conductivity of polymer nanocomposites.

where t is the time, m_i, r_i, F_i, U_i are the mass, position, force, and potential energy of atom i, respectively. The phonons in MD are considered to obey Maxwell Boltzmann distribution, which is invalid at low temperature. Hence MD isn't suitable for system with high Debye temperature. In order to overcome the size effect, the periodic boundary condition is likely to be used. When the system reaches the equilibrium state, the macroscopic property can be acquired according to statistical physics.

The microscopic connection is provided via the notion of an ensemble, which is an imaginary collection of systems described by the same Hamiltonian with each system in a unique microscopic state at any given instant in time. One of the basic ensembles is the microcanonical ensemble, whose Hamilton's equation conserves the total Hamiltonian

$$\mathcal{H}(r) = E \qquad (3.2)$$

The microcanonical ensemble consists of all microscopic states on the constant energy hypersurface determined by eqn. (3.2). The ensemble average of an observable $\mathcal{A}$ by a phase space function $\alpha(r)$ is given by

$$\mathcal{A} = <\alpha> = \int dr\, a(r)\delta(\mathcal{H}(r) - E)/\int dr\, \delta(H(r) - E) \qquad (3.3)$$

Based on ergodic hypothesis, the microcanoical phase space averages can be equivalent to time averages over the trajectory according to

$$\mathcal{A} = <\alpha> = \lim_{t\to\infty} \frac{1}{t}\int_0^t a\, dt \qquad (3.4)$$

One thing needs to note is that a single dynamical trajectory conveys little information because a slight change in initial conditions can change the trajectory dramatically. Observables require averaging over an ensemble of trajectories each with different initial conditions. Other equilibrium ensemble like canonical ensemble can be derived from microcanonical ensemble through Legendre transformation. All statistical ensembles are equivalent in the thermodynamic limit.[121]

Thermostat can be used in MD simulation to maintain the temperature of the system. The Nosé-Hoover thermostat and Langevin thermostat are two commonly used thermostats. The former is a global thermal bath while the latter is a local thermal bath. With respect to Nosé-Hoover chain algorithms are implemented to tune the temperature of the system and can generate a correct canonical distribution. The equation of atomic motion can be written as[122]

$$\sum_{i=1}^{N} \frac{1}{2} m_i |v_i|^2 = \frac{3}{2} N k_B T(t) \qquad (3.5)$$

$$\frac{d}{dt}(m_i v_i) = -\frac{\partial H}{\partial r_i} - \zeta m_i v_i \qquad (3.6)$$

$$\frac{d\zeta}{dt} = \frac{1}{\tau^2}\left[\frac{T(t)}{T_0} - 1\right] \qquad (3.7)$$

where ζ is the deterministic damping term and τ is the relaxation time. The Langevin thermostat is a stochastic thermal bath whose temperature-control equation can be written as

$$\frac{d}{dt}(m_i v_i) = -\frac{\partial H}{\partial r_i} + \xi - \gamma m_i v_i \qquad (3.8)$$

where ξ is the random force and γ is the dissipation rate. Compared with the Nosé-Hoover thermostat, the Langevin thermostat is more suitable to generate a linear temperature profile with small temperature jump.[48]

3.3 Spectral decomposition in non-equilibrium molecular dynamics simulation

Phonons are the main heat carriers in dielectric polymers and polymer nanocomposites, which are essentially wave packets.[9] Hence understanding thermal transport from the frequency perspective can deliver deep insights. Spectral decomposition methods based on lattice dynamics usually need eigenvectors and eigenvalues as inputs, which strongly limit their application in polymers. However, spectral decomposition methods based on NEMD don't have these limitations, which can be used as a powerful tool to unravel the underlying mechanisms about thermal transport in polymers.

The core of spectral decomposition is to acquire frequency-dependent heat current $Q(\omega)$. Hence the frequency-dependent ITC $G(\omega)$ can be defined as

$$G(\omega) = \frac{Q(\omega)}{A\Delta T} \qquad (3.9)$$

Similarly, the frequency-dependent thermal conductivity $\kappa(\omega)$ can be written as

$$\kappa(\omega) = \frac{Q(\omega)}{A\nabla T} \qquad (3.10)$$

For two-body potential, the heat current between atoms s and s′ (belong to chunk A and chunk B, respectively) can be written as[123-125]

$$Q_{s'\to s} = -Q_{s\to s'} = \frac{1}{2}<F_{ss'}\cdot(v_s + v_{s'})> \qquad (3.11)$$

where $F_{ss'}$ is the interatomic force between atoms s and s'; v_s and $v_{s'}$ are the velocity of atoms s and $v_{s'}$, respectively. The auxiliary correlation function for interparticle heat current can be defined as[126]

$$K_{s\to s'}(t) = -\frac{1}{2}<F_{ss'}(t)\cdot(v_s(0) + v_{s'}(0))> \qquad (3.12)$$

The total heat current between chunk A and chunk B can be written as

$$Q_{A\to B} = -Q_{B\to A} = -\frac{1}{2}\sum_{s\in A}\sum_{s'\in B}<F_{ss'}\cdot(v_s + v_{s'})> \qquad (3.13)$$

The auxiliary correlation function for total heat current between chunk A and chunk B can be written as

$$K_{A\to B}(t) = -\frac{1}{2}\sum_{s\in A}\sum_{s'\in B}<F_{ss'}(t)\cdot(v_s(0) + v_{s'}(0))> \qquad (3.14)$$

For many-body potential, the heat current between atoms s and s′ depends on the atoms' neighbor and cannot be simply described by Eqs. (3.11). Fortunately, a well-defined many-body heat current formula has been derived by Fan et al[127]

$$Q_{s'\to s} = -Q_{s\to s'} = <\frac{\partial U_s}{\partial r_{ss'}}\cdot v_{s'} - \frac{\partial U_{s'}}{\partial r_{s's}}\cdot v_s> \qquad (3.15)$$

where U_s and $U_{s'}$ are the site potential of atoms s and s′, respectively. $r_{ss'}$ is the relative position and can be written as

$$r_{ss'} = r_{s'} - r_s \qquad (3.16)$$

With respect to many-body potential, the auxiliary correlation function for interparticle heat current can be given by

$$K_{s\to s'}(t) = -<\frac{\partial U_s}{\partial r_{ss'}}(t)\cdot v_{s'}(0) - \frac{\partial U_{s'}}{\partial r_{s's}}(t)\cdot v_s(0)> \qquad (3.17)$$

The total heat current between chunk A and chunk B can be given by

$$Q_{A\to B} = -Q_{B\to A} = \sum_{s\in A}\sum_{s'\in B}Q_{s\to s'} =$$
$$-\sum_{s\in A}\sum_{s'\in B}<\frac{\partial U_s}{\partial r_{ss'}}\cdot v_{s'} - \frac{\partial U_{s'}}{\partial r_{s's}}\cdot v_s> \qquad (3.18)$$

The auxiliary correlation function for total heat current between chunk A and chunk B can be given by

$$K_{A\rightarrow B}(t) = -\frac{1}{2}\sum_{s\in A}\sum_{s'\in B}<\frac{\partial U_s}{\partial r_{ss'}}(t)\cdot \upsilon_{s'}(0) - \frac{\partial U_{s'}}{\partial r_{s's}}(t)\cdot \upsilon_s(0)> \quad (3.19)$$

The Fourier transformation pairs about the auxiliary correlation function can be defined as[127-129]

$$\widetilde{K}_{A\rightarrow B}(\omega) = \int_{-\infty}^{+\infty} K_{A\rightarrow B}(t)\, e^{-i\omega t} dt \quad (3.20)$$

$$K_{A\rightarrow B}(t) = \frac{1}{2\pi}\int_{-\infty}^{\infty} \widetilde{K}_{A\rightarrow B}(\omega)\, e^{i\omega t} d\omega \quad (3.21)$$

Since $K_{A\rightarrow B}(t)$ is real, the spectrally decomposed heat current between chunk A and chunk B can be written as

$$Q_{A\rightarrow B}(\omega) = 2Re[\widetilde{K}_{A\rightarrow B}(\omega)] \quad (3.22)$$

The phonon transmission function $\mathcal{T}(\omega)$ between chunk A and chunk B can be further defined as[130]

$$\mathcal{T}(\omega) = Q_{A\rightarrow B}(\omega)/k_B\Delta T \quad (3.23)$$

In order to distinguish elastic and inelastic spectral thermal conductance, Saaskilahti et al[128] and Zhou et al[131] propose to use second-order force constants and third-order force constants when calculating spectral heat current. Fig. 10 displays the typical spectrally decomposed heat current, thermal conductance, thermal conductivity and phonon transmission function. It can be seen that the spectral decomposition methodology has been successfully applied in crystalline material such as graphene and CNT. However, applying spectral decomposition method to thermal transport in polymers has been little reported. It will be hopeful to reveal the complex mechanism about thermal transport of polymers with the help of spectral decomposition method.

3.4 Molecular dynamics simulation in heat transfer
According to fluctuation-dissipation theorem[134] and linear response theory,[135-137] thermal conductivity can be calculated by Green-Kubo formula in equilibrium molecular dynamics (EMD) simulation

$$\kappa_{\alpha\beta} = \frac{1}{k_BVT^2}\int_0^\infty <J_\alpha(0)J_\beta(t)> dt \quad (3.24)$$

For two body potential, heat current $\mathbf{J}_{pair}$ can be defined as

$$\mathbf{J}_{pair} = \sum_i \upsilon_i E_i + \frac{1}{2}\sum_i\sum_{j\neq i} r_i[\mathbf{F}_{ij}\cdot(\upsilon_j - \upsilon_i)] \quad (3.25)$$

For many body potential, heat current can be defined as[138,139]

$$\mathbf{J}_{many} = \sum_i \upsilon_i E_i + \frac{1}{2}\sum_i\sum_{j\neq i} \mathbf{r}_{ji}(\frac{\partial U_i}{\partial \mathbf{r}_{ij}}\cdot \upsilon_j - \frac{\partial U_j}{\partial \mathbf{r}_{ji}}\cdot \upsilon_i) \quad (3.26)$$
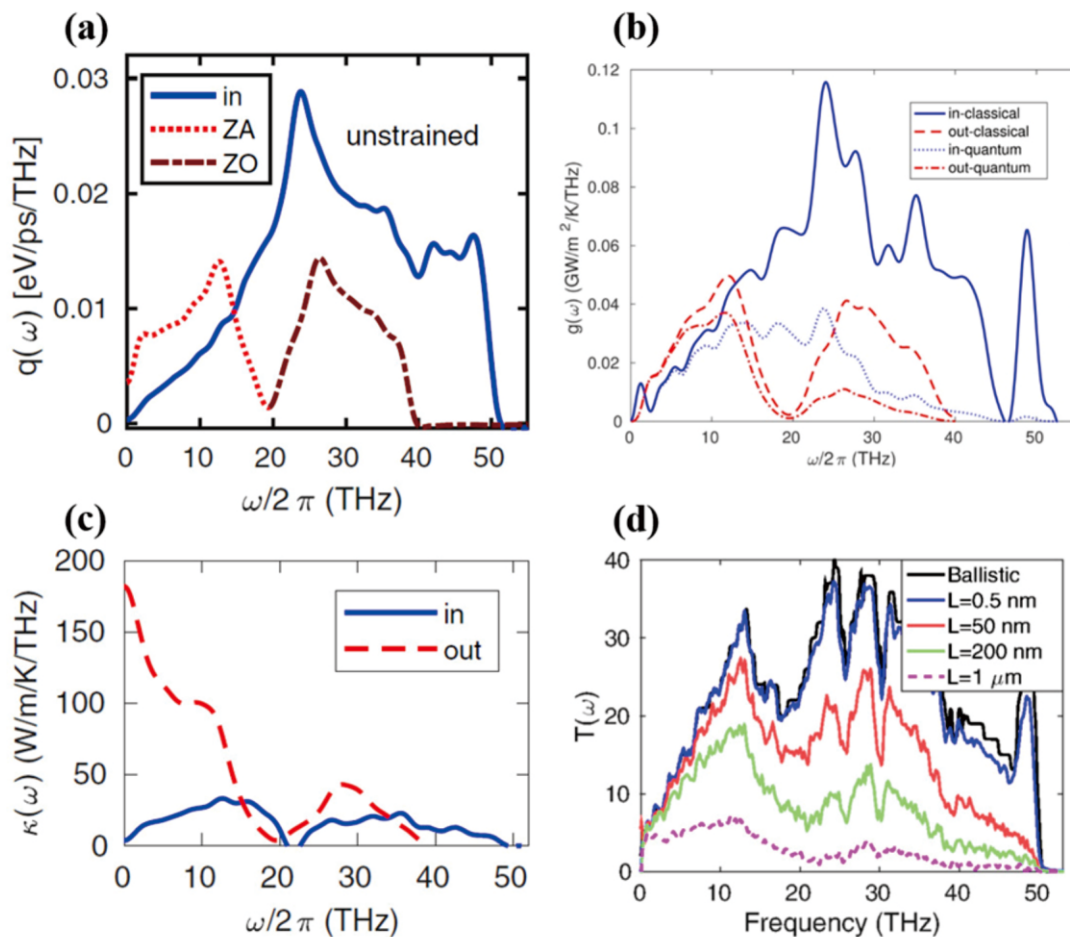
Fig. 10 Typical spectrally decomposed physical quantity. (a) Spectrally decomposed heat current of graphene.[127] Copyright 2017 American Physical Society. (b) Spectrally decomposed thermal conductance of polycrystalline graphene.[132] Copyright 2017 American Chemical Society. (c) Spectrally decomposed thermal conductivity of graphene.[133] Copyright 2019 American Physical Society. (d) Phonon transmission spectra of CNT.[130] Copyright 2019 American Physical Society.

Apart from EMD, thermal conductivity can also be calculated by NEMD simulation in conjunction with Fourier's law. Dong and Fan *et al* have demonstrated that EMD and NEMD are essentially equivalent in terms of computing thermal conductivity.[140] Fig. 11 displays the useful methods to enhance thermal conductivity of polymers in MD simulation, including mechanical stretching, molecular layer deposition, increasing the stiffness of backbone and forming hydrogen bond.

Meng and Yang *et al* discover that thermal conductivity of polymers is strongly associated with the morphology.[143] The aforementioned methods can align the polymer chain, increase the length of thermal conductive path, and reduce the structural disorder and thus facilitate thermal transport in polymers. The thermal conductivity of typical sample and computing methodology are listed in Table 2.

It can be seen that the thermal conductivity of polymers is strongly related to the potential function. The all-atom potential like PCFF and COMPASS is usually more accurate than united-atom potential like OPLS-UA. The accurate potential often means time-consuming computation. Researchers need to consider the accuracy and computational cost. Secondly, the thermal conductivity of single polymer chains is always higher than bulk polymers due to less phonon scattering. Compared with amorphous polymers, thermal conductivity of crystalline polymers is always higher due to well-organized structure. Thermal energy can transport more effectively along polymer backbones. Excessive branching can cause more phonon scattering, thus is unfavorable for heat transport. Therefore, polymers with less side chains, aligned molecular chains, ordered structure are desired thermal conductive material.

Apart from tuning the intrinsic thermal conductivity of polymers, doping high thermal conductive fillers is another popular way to increase the thermal conductivity of polymers. As previously mentioned, the major barrier to fabricate thermal conductive polymer nanocomposites is the ITR between fillers and matrix. The ITC between typical fillers and matrix is shown in Table 3.

As can be seen from Table 3, the ITC also depends on the computational method and potential function. Therefore, it is necessary to check the potential function before the simulation. In addition, the ITC is related to the contact area, binding energy and molecular polarity. Generally speaking, covalent connections can be more efficient to enhance the ITC than nonconvalent connections. Nevertheless, covalent bonding can damage the intrinsic structure of the fillers. SAMs with the similar backbone to the matrix can protect the fillers and be used as the phonon bridge to increase the vibrational coupling, which can effectively enhance the thermal transport across the interface.

4. Experimental advances in fabricating high thermal conductive polymers

High thermal conductive polymers have been realized not only in simulations but also in experiments. Fig. 12 displays the typical preparation methods including mechanical stretching, electrospinning and molecular engineering. The common mechanism behind these methods is that they can increase the alignment of polymer chains. In addition, when applying large strain to the sample, mechanical stretching can elevate the crystallinity of sample. Electrospinning is a popular method to prepare polymer fibers. Molecular engineering can modulate thermal transport property of polymers from the molecular level, which can be used in conjunction with electrospinning technology to fabricate high thermal conductive polymers. The typical preparation methods, samples and corresponding thermal conductivity are listed in Table 4.

As shown in Fig. 12(a), Shen *et al* fabricated ultra-drawn PE nanofibers with extremely high thermal conductivity.[6] Kim *et al* fabricated high thermal conductive polyacrylic acid (PAA) film with the help of coulombic force[172]. Singh *et al* fabricated high thermal conductive polythiophene nanofibers by nanoscale templates.[12] Xu and Chen *et al* fabricated high thermal conductive PE film by employing flow extrusion and mechanical strain.[159] The common point here is to
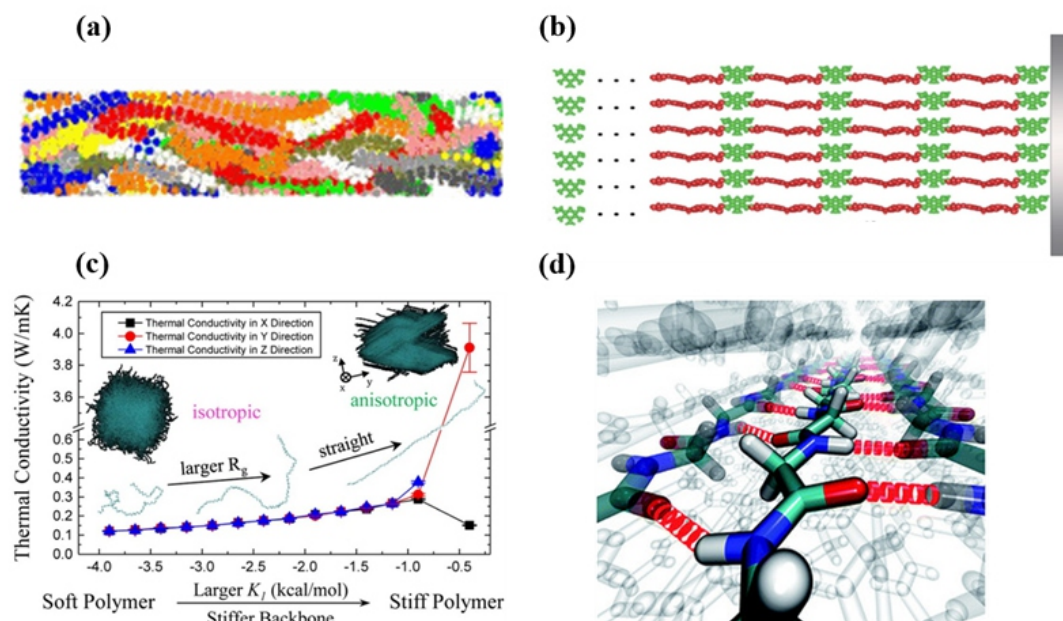
Fig. 11 Enhancing thermal conductivity of polymers by different methods. (a) Mechanical strain.[141] Copyright 2010 American Physical Society. (b) Construct parallel-linked epoxy resin by molecular layer deposition.[108] Copyright 2018 American Chemical Society. (c) Increase the stiffness of polymer backbone.[111] Copyright 2016 American Chemical Society. (d) Confine structural disorder by forming hydrogen bond.[142] Copyright 2015 Royal Society of Chemistry.

increase the polymer chain orientation.

Fig. 12(b) shows that the process of preparing PE nanofibers with both high strength and thermal conductivity by local heating method.[8] Cahill[7] *et al* measured thermal conductivity of different fibers like PE, PVA, PAA etc. They discovered that the polymers with higher strength have higher thermal conductivity.[7,179] Zhu *et al* fabricated high thermal conductive PVA/Fe$_3$O$_4$ composites in conjunction with magnetic field. The common underlying mechanism is that the higher mechanical strength leads to higher sound speed, which can facilitate thermal transport in polymers.

Fig. 12(c) and (d) display the vertical set up of electrospinning and oriented PE chains in the electrospinning process, respectively. Ma and Li *et al* discover that the thermal conductivity of electrospun polymer nanofiber is associated with the electric field.[158] The electric filed can influence the arrangement of polymer chains, which may lead to scattered thermal conductivity of electrospun nanaofibers.

Polymer blends with high thermal conductivity can be prepared by forming strong interchain bonds.[113] Zhu *et al* fabricated high thermal conductive films by employing small organic linkers.[180] The underlying mechanism is that strong interchain interaction promotes phonon transport.[181] Apart from interchain interaction, intrachain interaction also plays an important role in thermal transport. As shown in Fig. 12(e), Xu and Chen *et al* fabricated high thermal conductive conjugated polymers by simultaneously tuning intrachian interaction and interchain interaction.[114] The high thermal conductivity results from efficient thermal conductive network in conjugated polymers.

Table 2 Thermal conductivity of typical sample and simulation details.

Sample	κ(W/m^{-1}K^{-1})	Computing method	Potential function	Refs
Single PE chains	350	EMD	AIREBO	[4]
Bulk PE crystals	237	ALD		[144]
DPG-1 zigzag	84.4	EMD	PCFF	[145]
DPG-1 armchair	110.8	EMD	PCFF	[145]
Aligned CNT-PE	99.5	NEMD	Morse + cosine + LJ + AIREBO	[14]
Crystalline PEO	60	EMD	PCFF	[143]
Twisted PE chains	60	EMD	AIREBO	[146]
Bulk single PE crystal	50	EMD	AIREBO	[147]
Single PT chains	43.3	EMD	ReaxFF	[12]
Nylon 10	7.83	NEMD	OPLSAA	[142]
Single PVA chains	7.01	EMD	COMPASS	[68]
Single PDMS chain	6	NEMD	COMPASS	[148]
Single PP chains	5.83	EMD	COMPASS	[68]
Aligned single PNb chains	2.54	EMD	PCFF	[109]
PAAm hydrogels	0.98	EMD	OPLS + TIP4P	[149]
Parallel-linked epoxy resin	0.8	EMD	CVFF	[108]
Bulk PNb crystal	0.72	EMD	PCFF	[150]
Amorphous PEO	0.37	EMD	PCFF	[143]
Amorphous paraffin wax	0.332	NEMD	AIREBO	[13]
Amorphous paraffin wax	0.327	NEMD	COMPASS	[13]
Amorphous PT	0.3	EMD	ReaxFF	[5]
Crystalline PE	0.26 (radial)	NEMD	PCFF	[151]
Amorphous PS film	0.249	EMD	CVFF	[152]
Amorphous PE	0.27	NEMD	NERD united potential	[153]
Amorphous PE	0.22	NEMD	COMPASS	[141]
Amorphous PDMS	0.2	NEMD	COMPASS	[148]
Amorphous PS	0.17	EMD	PCFF	[109]
Amorphous PS	0.16	NEMD	PCFF	[153]
Amorphous PE	0.14 (600K)	NEMD	OPLS-UA	[154]
Amorphous PP	0.07 (600K)	NEMD	OPLS-UA	[154]

Compared with the simulation, measuring the ITC in experiment is arduous due to the such small sample, expensive equipment and scrupulous operation. The electrothermal 3ω method, pump/probe thermoreflectance techniques like time-domain thermoreflectance (TDTR) and frequency-domain thermoreflectance (FDTR) are the predominant methods to measure the ITC.[182] The typical experimental results are listed in Table 5.

As can be seen from table 5, the typical ITC between polymers and fillers is in the range of 5~170 MWm^{2}K^{-1}. The SAMs with different end-group molecules can have different effects on the interfacial thermal transport. SAMs that form strong interaction with the matrix often facilitate interfacial thermal transport, whereas SAMs that still keep weak interaction with the matrix can impede interfacial thermal transport. The simulations and experimental results confirm that the SAMs can be a good candidate to enhance interfacial thermal transport.

5. Summary and outlook

For thermal transport in crystalline materials, lattice dynamic theory can help us to understand the underlying mechanisms very well. However, thermal transport in amorphous material is still not well understood. Although A-F theory provides a useful methodology to specify important carriers to thermal transport, distinguishing propagons and diffusons is insurmountable for large size systems. Some theoretical models have been proposed to understand the interfacial thermal transport and calculate the interfacial thermal conductance. Nevertheless, these models often need to input the eigenvector, eigenfrequency, and phonon group velocity. For polymers with many atoms in supercell, the lattice dynamic calculation is often intractable due to huge amount of calculation. The emergence of thermal rectification provides hope for manipulating the heat current while the low thermal rectification ratio and expensive cost hinder the

Table 3 Interfacial thermal conductance between typical fillers and polymer matrix.

Fillers	Matrix	$G(MWm^{-2}K^{-1})$	Computing method	Potential function	Refs
Graphene	Epoxy	135.53	NEMD	PCFF	[71]
Graphene with Stone-Wales defect	Epoxy	162.642	NEMD	PCFF	[71]
Graphene	PE	136.2	NEMD	ReaxFF	[155]
Graphene	Paraffin	71	NEMD	AIREBO+COMPASS	[13]
Graphene	PE	56	NEMD	PCFF	[156]
BN	Hexane	90.47	NEMD	Tersoff+PCFF	[57]
BN	Hexanamine	113.38	NEMD	Tersoff+PCFF	[57]
BN	Hexanol	136.16	NEMD	Tersoff+PCFF	[57]
BN	Hexanoic acid	155.17	NEMD	Tersoff+PCFF +UFF	[57]
Gold + CH_3 SAM	Hexylamine	55.33	EMD	Morse+PCFF +UFF	[81]
Gold + hetero-length SAMs	Hexylamine	92.85	EMD	Tersoff+PCFF +UFF	[81]
Gold + hetero-length SAMs	Propylamine	102.11	EMD	Morse+PCFF +UFF	[81]
Gold + hetero -CH_3 SAMs	Hexylamine	109.60	EMD	Morse+PCFF +UFF	[81]
Gold + pseudo-hetero-length SAMs	Hexylamine	120.13	EMD	Tersoff+PCFF +UFF	[81]
Gold + mixed short SAMs	Hexylamine	168.75	EMD	Morse+PCFF +UFF	[81]
Gold + COOH SAMs	Hexylamine	208.78	EMD	Morse+PCFF +UFF	[81]
Gold + CH_3 SAMs	Hexane	55.18	EMD	Tersoff+PCFF +UFF	[81]
Gold + COOH SAMs	Hexane	73.76	EMD	Morse+PCFF +UFF	[81]

applications. Powerful computational methods can accelerate the research on thermal properties of materials. The thermal conductivity can be obtained according to Green-Kubo relations in EMD simulation or Fourier's law in NEMD simulation. However, accurate potentials are essential to get the accurate thermal conductivity, which will consume large amount of computing resource due to the complicated potentials and vast neighbor atoms. Furthermore, multiple independent simulations are necessary to get the thermal conductivity with small standard error. Advanced spectral decomposition methods are introduced to assist us to reveal the phonon transport mechanism inside the material and at the interface. High thermal conductive polymers and polymer nanocomposites have been fabricated in experiments, which promotes the practical applications of thermal conductive polymers. Some consensuses have been reached on enhancing thermal conductivity of polymers, like aligning the polymer chain, increasing the stiffness of polymer backbone, restricting the angular bending freedom, and elevating the crystallinity of polymers,

However, there still remain some open questions. First and foremost, the experimentally measured thermal conductivity and interfacial thermal conductance results are scarce, especially for low dimensional polymers like one-dimensional polymer chain and two-dimensional polymer films. Only a few papers report the thermal conductivity of low dimensional polymers at room temperature. Preparing low dimensional polymers and measuring their thermal conductivities still remain challenges. The scattering simulation results sometimes contain numerical tricks and can't provide effective guidance to design high thermal conductive polymers. The accurate experimental results can efficiently complement the shortages of the simulation and speed up the industrialization of the thermal conductive polymers. Therefore, developing feasible method to overcome the experimental challenges will be a research focus. Secondly, the reliable and pragmatic theoretical model that can accurately predict the thermal conductivity of polymers and polymer nanocomposites is still lacking. The results based on the empirical relations can reflect a general trend and fail to produce
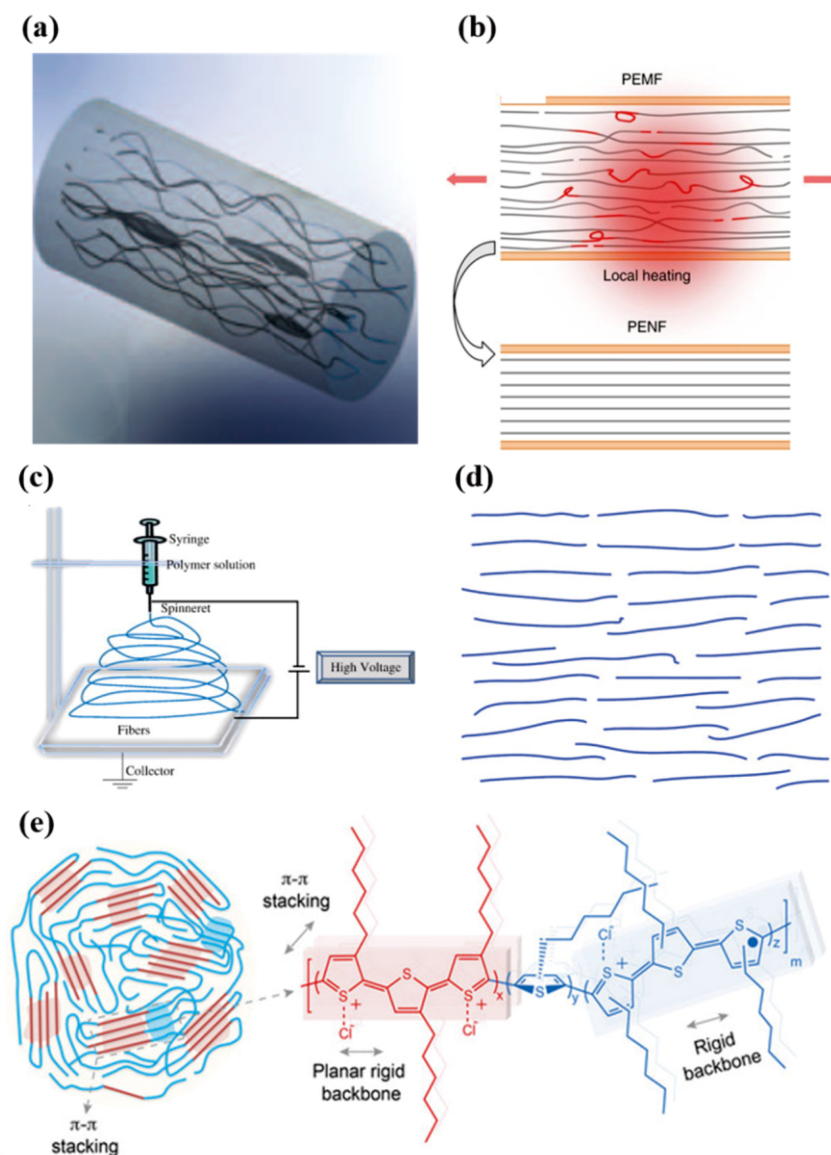
Fig. 12 Fabricate high thermal conductive polymers in experiments. (a) Schematic of stretched PE microfiber.[6] Copyright 2010 Nature Publishing Group. (b) Fabricating PE nanofibers from PE microfibers by local heating and drawing.[8] Copyright 2018 Nature Publishing Group. (c) Schematic of electrospinning equipment.[157] Copyright 2010 Elsevier Ltd. (d) Aligned PE chains in the electrospinning process.[158] Copyright 2015 Royal Society of Chemistry. (e) Schematic of polymers with rigid backbone and strong inter-chain interaction.[114] Copyright 2018 AAAS.

the precise thermal conductivity value. The NEMD simulation for small system is often accompanied by large temperature gradient on the order of 10^9 K/m, which is extremely rare in the realistic situation. In addition, the simulation results don't always agree with the experimental results due to the complicated simulation details like suitable initial structure, proper boundary condition, accurate potential function, rational time step and enough simulation time. Phonons are considered to obey Maxwell-Boltzmann distribution in MD simulation whereas phonons obey Bose-Einstein distribution in reality. Hence the theory of MD simulation needs to be further developed to have more physical meaning and to agree with the simulation result. Thirdly, large interfacial thermal resistance at the material interface is still a bottleneck in enhancing thermal conductivity of polymer nanocomposites. Novel strategies to reduce interfacial thermal resistance are still worthwhile to develop. Although polymer nanofibers can have high thermal conductivity along the chain, the thermal transport vertical to the chain is still unsatisfactory. Isotropic polymers with high thermal conductivity needs to be prepared. Finally, in order to apply thermal rectification in thermal management, more investment are needed to study polymer thermal diode in experiment.

Acknowledgements

Conflict of interest

The authors declare no financial interest.

Table 4 Typical samples, thermal conductivity and preparation methods.

Sample	κ (W/m^{-1}K^{-1})	Preparation method	Refs
Ultra-drawn PE nanofibers	104	Two-stage heating and drawing	[6]
Crystalline PE nanofibers	90 (150K)	Local heating and drawing	[8]
PE films	62	Flow extrusion and drawing	[159]
UHMW PE microfibers	51	Heat-stretching method	[160]
Liquid crystalline PBO fibers	20	Embedding fibers and micro dissection	[7]
PEO naofibers	13~29	Electrospinning	[161]
PVDF/BNN S film	16.3	Electrospi nning	[162]
HDPE nanowire arrays	10	Nanoporous template wetting	[107]
Electrospun PE nanofibers	9.3	Electrospinning	[158]
HDPE nanofibers	9	Melt infiltration of AAO templates	[163]
Cross-linked LCER	5.8	Surface treatment	[164]
P3HT/MWCNT nanofibers	4.7	Template method	[165]
PMDA/ODA nanofibers	4.6	Electrospinning	[166]
Epoxy resin/3D CNT	4.42	Ice-templating SAM and infiltration	[167]
Amorphous PT nanofibers	4.4	Nanoscale templates	[12]
HDPE/BN	3.57	Melt extrusion	[168]
P3HT film	2.2	Oxidative chemical vapor deposition	[114]
Nylon 11 nanofibers	1.6	Electrospinning and post-stretching	[169]
Electrospun PVA nanofibers	1.5	Electrospinning	[170]
PAP:PAA blend fims	1.5	Mixing method	[113]
PMMA -BNNS/Ag	1.48	Solution -blending	[171]
Amorphous PAA films	1.2	Systematic ionization	[172]
PAI/3D BN	1.17	cross-linking - freeze -drying- infiltration	[173]
Diamond -ABS filament	0.94	3D printing	[174]
PVA membrane	0.7	Electrospinning	[175]
PVA/Fe$_3$O$_4$ films	0.63	Film casting and magnetic alignment	[176]
PAAm hydrogels	0.51	Free radicals copolymerization method	[177]
Ordered LCER	0.48	Linear polymerization of the epoxy	[178]

Table 5 Typical interfacial thermal conductance and measuring methods.

Sample	$G\,(MWm^{-2}K^{-1})$	Measuring method	Refs
Cooper/epoxy	12.5	Thermal measurements	[183]
Cooper/ SAM-CH$_3$/ epoxy	7.1	Thermal measurements	[183]
Cooper/ SAM-NH$_2$/ epoxy	142.9	Thermal measurements	[183]
CNT/hydrocarbon liquid	12	Laser measurement	[184]
BN/epoxy	13.2	Laser flash method	[185]
Magnetic oriented BN/epoxy	120.5	Laser flash method	[185]
Au/paraffin wax	25	Transient thermoreflectance	[78]
Au/hexadecane	28	Transient thermoreflectance	[78]
Au/ alkanethiol SAMs/ paraffin wax	165	Transient thermoreflectance	[78]
Au/ alkanethiol SAMs/ hexadecane	169	Transient thermoreflectance	[78]
Au/ethanol	17.7	TDTR	[186]
Au/toluene	13.8	TDTR	[186]
Sapphire/ PS	7.6	TDTR	[187]
Sapphire/ silane SAM /PS	58	TDTR	[187]
Al/PS	19.35	TDTR	[188]
Si/PS	16.28	TDTR	[188]
Al/PMMA	30	3ω	[189]
Sapphire/ HDPE	5	TDTR	[190]
Sapphire/ PS	7.0~21.0	TDTR	[191]

Nomenclature

κ_e	electronic thermal conductivity		$\bar{\upsilon}_g$	average phonon group velocity
κ_{ph}	phononic thermal conductivity		τ	phonon relaxation time
κ_{pr}	propagons' thermal conductivity		Λ	phonon mean free path
κ_{dif}	diffusons' thermal conductivity		$\hbar$	reduced Planck's constant
κ_{lo}	locons' thermal conductivity		$\mathbf{q}$	phonon wave vector
κ_+	forward thermal conductivity		j	phonon polarization
κ_-	backward thermal conductivity		ω	phonon frequency
κ	total thermal conductivity		$\mathbf{e}$	eigenvector
J$_+$	forward heat flux		f_{BE}	Bose-Einstein distribution
J$_-$	backward heat flux		Φ	force constant matrix
J	heat flux		$\mathbf{D(q)}$	dynamical matrix
Q	heat current		Di	mode diffusivity
G	thermal conductance		$\mathcal{T}$	transmissivity
A	cross-sectional area		η	thermal rectification ratio
∇T	temperature gradient		U	potential energy function
ΔT	temperature difference		E	total energy
C$_v$	volumetric specific heat		$\mathcal{H}$	Hamiltonian
υ_g	phonon group velocity		υ	atomic velocity

$\mathcal{A}$	observable property
α	phase space function
δ	Dirac δ-function
ζ	damping term
ξ	random force
γ	dissipation rate
ABS	acrylonitrile butadiene styrene
LCER	liquid crystalline epoxy resin
PA	polymide
PA6	nylon-6
PA66	nylon-6.6
PAA	polyacrylic acid
PAI	Polyamide-imide
PAAm	poly (acrylamide)
PAP	poly (n-acryloyl piperidine)
PBO	polybenzobisoxazole
PE	polyethylene
PEX	cross-linked polyethylene
LDPE	low-density polyethylene
HDPE	high-density polyethylene
PDMS	poly(dimethylsiloxane)
PI	polyimide
PMMA	poly(methylmethacrylate)
PNb	polynorborn ene
P3HT	poly (3-hexylthiophene)
PP	polypropylene
PS	polystyrene
PT	polythiophene
PVC	polyvinyl chloride
PVDF	polyvinylidene fluoride
BAs	boron arsenide
BN	boron nitride
BNNS	boron nitride nano-sheets
AAO	anodic aluminum oxide
Ag	silver
Au	gold
CNT	carbon nanotube
MWCNT	multiwalled carbon nanotube
DPG	dubbed porous graphene
SiC	silicon carbide
GaN	gallium nitride
Ge	germanium
SAM	self-assembled monolayer
PnCs	phononic crystals
BB	bottlebrush

IL	intermediate layer
LJ	Lennard-Jones
BTE	Boltzmann transport equation
AGF	atomistic Green's function
ALD	anharmonic lattice dynamics
MD	molecular dynamics
EMD	equilibrium molecular dynamics
NEMD	non-equilibrium molecular dynamics
DOS	density of states
PR	participation ratio
EP	eigenvector periodicity
LR	localization ratio
ITC	interfacial thermal conductance
ITR	interfacial thermal resistance
TR	thermal rectification
TDTR	Time-domain thermoreflectance
FDTR	Frequency-domain thermoreflectance
VACF	velocity autocorrelation function
VPS	vibrational power spectra
UHMW	ultrahigh-molecular-weight
AIREBO	Adaptive intermolecular reactive empirical bond order potential
COMPASS	Condensed-phase optimized molecular potentials for atomistic simulation studies
CVFF	Consistent valence force field
OPLS-AA	Optimized potential for liquid simulations all atom model
OPLS-UA	Optimized potential for liquid simulations-united atom model
PCFF	Polymer consistent force field
ReaxFF	Reactive force-field

References

1. J. E. Mark, *Physical Properties of Polymer Handbook*, Springer: New York, 2007.
2. H. Chen, V. V. Ginzburg, J. Yang, Y. Yang, W. Liu, Y. Huang, L. Du and B. Chen, *Prog. Polym. Sci.*, 2016, **59**, 41-85.
3. Z. Han and A. Fina, *Prog. Polym. Sci.*, 2011, **36**, 914-944.
4. A. Henry and G. Chen, *Phys. Rev. Lett.*, 2008, **101**, 235502.
5. W. Lv, R. M. Winters, F. D. Angelis, G. Weinberg and A. Henry, *J. Phys. Chem. A*, 2017, **121**, 5586-5596.
6. S. Shen, A. Henry, J. Tong, R. Zheng and G. Chen, *Nat. Nanotechnol*, 2010, **5**, 251.
7. X. Wang, V. Ho, R. A. Segalman and D. G. Cahill, *Macromolecules*, 2013, **46**, 4937-4943.
8. R. Shrestha, P. Li, B. Chatterjee, T. Zheng, X. Wu, Z. Liu, T. Luo, S. Choi, K. Hippalgaonkar, M. P. de Boer and S. Shen, *Nat. Commun.*, 2018, **9**, 1664.
9. J. M. Ziman, *Electrons and phonons: the theory of transport phenomena in solids*, Oxford university press, 2001.
10. G. Chen, *Nanoscale Energy Transport and Conversion: A Parallel Treatment of Electrons, Molecules, Phonons, and Photons*, Oxford University Press, 2005.
11. M. Kaviany, *Heat transfer physics*, Cambridge University Press, 2014.
12. V. Singh, T. L. Bougher, A. Weathers, Y. Cai, K. Bi, M. T. Pettes, S. A. McMenamin, W. Lv, D. P. Resler, T. R. Gattuso, D. H. Altman, K. H. Sandhage, L. Shi, A. Henry and B. A. Cola, *Nat. Nanotechnol*, 2014, **9**, 384.
13. T. Luo and J. R. Lloyd, *Adv. Funct. Mater.*, 2012, **22**, 2495-2502.
14. Q. Liao, Z. Liu, W. Liu, C. Deng and N. Yang, *Sci. Rep.*, 2015, **5**, 16543.

15. C. Yuan, B. Duan, L. Li, B. Xie, M. Huang and X. Luo, *ACS Appl. Mater. Interfaces*, 2015, **7**, 13000-13006.

16. J. Zhu, K. Hippalgaonkar, S. Shen, K. Wang, Y. Abate, S. Lee, J. Wu, X. Yin, A. Majumdar and X. Zhang, *Nano Lett.*, 2014, **14**, 4867-4872.

17. H. Liu, H. Wang and X. Zhang, *Appl. Sci.*, 2019, **9**, 344.

18. C. Huang, X. Qian and R. Yang, *Mater. Sci. Eng. R*, 2018, **132**, 1-22.

19. M. T. Dove and M. T. Dove, *Introduction to lattice dynamics*, Cambridge university press, Cambridge 2005.

20. R. E. Peierls, *Quantum theory of solids*, Clarendon Press, 1996.

21. C. Kittel, *Introduction to Solid State Physics*, 8th edn., John Wiley & Sons, 2005.

22. S. Iijima, *Nature*, 1991, **354**, 56-58.

23. A. K. Geim and K. S. Novoselov, *Nat. Mater.*, 2007, **6**, 183.

24. Y. Wang, N. Xu, D. Li and J. Zhu, *Adv. Funct. Mater.*, 2017, **27**, 1604134.

25. X. Gu, Y. Wei, X. Yin, B. Li and R. Yang, *Rev. Mod. Phys.*, 2018, **90**, 041002.

26. L. Lindsay, D. A. Broido, T. L. Reinecke, *Phys. Rev. Lett.*, 2013, **111**, 025901.

27. S. Li, Q. Zheng, Y. Lv, X. Liu, X. Wang, P. Y. Huang, D. G. Cahill and B. Lv, *Science*, 2018, **361**, 579.

28. J. S. Kang, M. Li, H. Wu, H. Nguyen and Y. Hu, *Science*, 2018, **361**, 575.

29. F. Tian, B. Song, X. Chen, N. K. Ravichandran, Y. Lv, K. Chen, S. Sullivan, J. Kim, Y. Zhou, T. H. Liu, M. Goni, Z. Ding, J. Sun, G. A. G. Udalamatta Gamage, H. Sun, H. Ziyaee, S. Huyan, L. Deng, J. Zhou, A. J. Schmidt, S. Chen, C. W. Chu, P. Y. Huang, D. Broido, L. Shi, G. Chen and Z. Ren, *Science*, 2018, **361**, 582.

30. Z. Pang, X. Gu, Y. Wei, R. Yang and M. S. Dresselhaus, *Nano Lett.*, 2017, **17**, 179-185.

31. O. Dubay and G. Kresse, *Phys. Rev. B*, 2003, **67**, 035401.

32. Y. Zhang, D. Ma, Y. Zang, X. Wang and N. Yang, *Front. Energy Res.*, 2018, **6**, 48.

33. N. Yang, X. Xu, G. Zhang and B. Li, *AIP Adv.*, 2012, **2**, 041410.

34. C. Shao, X. Yu, N. Yang, Y. Yue and H. Bao, *Nanosc. Microsc. Therm.*, 2017, **21**, 201-236.

35. T. Feng, B. Qiu and X. Ruan, *Phys. Rev. B*, 2015, **92**, 235206.

36. J. Guo, L. Dong, Q. Xi, Y. Li, X. Xu, J. Zhou, T. Nakayama, Z. Liang, D. Chen and B. Li, *NatI. Sci. Rev.*, 2018, **5**, 500-506.

37. P. B. Allen and J. L. Feldman, *Phys. Rev. Lett.*, 1989, **62**, 645-648.

38. J. L. Feldman, M. D. Kluge, P. B. Allen and F. Wooten, *Phys. Rev. B*, 1993, **48**, 12589-12602.

39. P. B. Allen, J. L. Feldman, J. Fabian and F. Wooten, *Phil. Mag. B*, 1999, **79**, 1715-1731.

40. P. B. Allen and J. L. Feldman, *Phys. Rev. B*, 1993, **48**, 12581-12588.

41. J. A. Tomko, A. Pena-Francesch, H. Jung, M. Tyagi, B. D. Allen, M. C. Demirel and P. E. Hopkins, *Nat. Nanotechnol*, 2018, **13**, 959-964.

42. W. Garber, F. M. Tangerman, P. B. Allen and J. L. Feldman, *Phil. Mag. Lett.*, 2001, **81**, 433-439.

43. J. M. Larkin and A. J. H. McGaughey, *Phys. Rev. B*, 2014, **89**, 144303.

44. H. R. Seyf and A. Henry, *J. Appl. Phys.*, 2016, **120**, 025101.

45. H. R. Seyf, L. Yates, T. L. Bougher, S. Graham, B. A. Cola, T. Detchprohm, M. H. Ji, J. Kim, R. Dupuis, W. Lv and A. Henry, *Npj Comput. Mater.*, 2017, **3**, 49.

46. D. Ma, H. Ding, H. Meng, L. Feng, Y. Wu, J. Shiomi and N. Yang, *Phys. Rev. B*, 2016, **94**, 165434.

47. G. C. Loh, E. H. T. Teo and B. K. Tay, *Diamond Relat. Mater.*, 2012, **23**, 88-92.

48. H. Bao, J. Chen, X. Gu and B. Cao, *ES Energy Environ.*, 2018, **1**, 16-55.

49. J. M. Dickey and A. Paskin, *Phys. Rev.*, 1969, **188**, 1407-1418.

50. L. Yang, N. Yang and B. Li, *Nano Lett.*, 2014, **14**, 1734-1738.

51. S. Shenogin, A. Bodapati, P. Keblinski and A. J. H. McGaughey, *J. Appl. Phys.*, 2009, **105**, 034906.

52. A. L. Moore and L. Shi, *Mater, Today*, 2014, **17**, 163-174.

53. N. Yang, T. Luo, K. Esfarjani, A. Henry, Z. Tian, J. Shiomi, Y. Chalopin, B. Li, G. Chen and *J. Comput. Theor. Nanosci.*, 2015, **12**, 168-174.

54. P. Zhang, P. Yuan, X. Jiang, S. Zhai, J. Zeng, Y. Xian, H. Qin and D. Yang, *Small*, 2018, **14**, 1702769.

55. N. Mehra, L. Mu, T. Ji, X. Yang, J. Kong, J. Gu and J. Zhu, *Appl. Mater. Today*, 2018, **12**, 92-130.

56. X. Xu, J. Chen, J. Zhou and B. Li, *Adv. Mater.*, 2018, **30**, 1705544.

57. R. Ma, X. Wan, T. Zhang, N. Yang and T. Luo, *ACS Omega*, 2018, **3**, 12530-12534.

58. D. G. Cahill, P. V. Braun, G. Chen, D. R. Clarke, S. Fan, K. E. Goodson, P. Keblinski, W. P. King, G. D. Mahan, A. Majumdar, H. J. Maris, S. R. Phillpot, E. Pop and L. Shi, *Appl. Phys. Rev.*, 2014, **1**, 011305.

59. D. G. Cahill, W. K. Ford, K. E. Goodson, G. D. Mahan, A. Majumdar, H. J. Maris, R. Merlin and S. R. Phillpot, *J. Appl. Phys.*, 2002, **93**, 793-818.

60. W. A. Little, *Can. J. Phys.*, 1959, **37**, 334-349.

61. E. T. Swartz and R. O. Pohl, *Rev. Mod. Phys.*, 1989, **61**, 605-668.

62. S. Hida, T. Hori, T. Shiga, J. Elliott and J. Shiomi, *Int. J. Heat Mass Transfer*, 2013, **67**, 1024-1029.

63. X. Wu and T. Luo, *J. Appl. Phys.*, 2014, **115**, 014901.

64. T. Feng, Y. Zhong, J. Shi and X. Ruan, *Phys. Rev. B*, 2019, **99**, 045301.

65. A. Giri and P. E. Hopkins, *Sci. Rep.*, 2017, **7**, 11011.

66. E. Lee and T. Luo, *Phys. Chem. Chem. Phys.*, 2017, **19**, 18407-18415.

67. N. Yang, G. Zhang and B. Li, *Nano Lett.*, 2008, **8**, 276-280.

68. Q. Liao, L. Zeng, Z. Liu and W. Liu, *Sci. Rep.*, 2016, **6**, 34999.

69. X. Li, J. Chen, C. Yu and G. Zhang, *Appl. Phys. Lett.*, 2013, **103**, 013111.

70. S. Hu, J. Chen, N. Yang and B. Li, *Carbon*, 2017, **116**, 139-144.

71. M. Li, B. Zheng, K. Duan, Y. Zhang, Z. Huang and H. Zhou, *J. Phys. Chem. C*, 2018, **122**, 14945-14953.

72. J. Al-Ghalith, Y. Ni and T. Dumitrică, *Phys. Chem. Chem. Phys.*, 2016, **18**, 9888-9892.

73. K. Termentzidis, M. Isaiev, A. Salnikova, I. Belabbas, D. Lacroix and J. Kioseoglou, *Phys. Chem. Chem. Phys.*, 2018, **20**, 5159-5172.

74. X. Liu, G. Zhang and Y. W. Zhang, *Nano Lett.*, 2016, **16**, 4954-4959.

75. A. Giri, S. W. King, W. A. Lanford, A. B. Mei, D. Merrill, L. Li, R. Oviedo, J. Richards, D. H. Olson and J. L. Braun, *Adv. Mater.*, 2018, **30**, 1804097.

76. C. F. Carlborg, J. Shiomi and S. Maruyama, *Phys. Rev. B*, 2008, **78**, 205406.

77. X. Yang, D. Yu and B. Cao, *ACS Appl. Mater. Interfaces*, 2017, **9**, 24078-24084.

78. F. Sun, T. Zhang, M. Jobbins Matthew, Z. Guo, X. Zhang, Z. Zheng, D. Tang, S. Ptasinska and T. Luo, *Adv. Mater.*, 2014, **26**, 6093-6099.

79. X. Wei, T. Zhang and T. Luo, *ACS Energ. Lett.*, 2017, **2**, 2283-2292.

80. T. Luo and J. R. Lloyd, *Int. J. Heat Mass Transfer*, 2010, **53**, 1-11.

81. X. Wei, T. Zhang and T. Luo, *ACS Appl. Mater. Interfaces*, 2017, **9**, 33740-33748.

82. B. Li, L. Wang and G. Casati, *Phys. Rev. Lett.*, 2004, **93**, 184301.

83. L. Wang and B. Li, *Phys. Rev. Lett.*, 2007, **99**, 177208.

84. L. Wang and B. Li, *Phys. Rev. Lett.*, 2008, **101**, 267203.

85. N. Li, J. Ren, L. Wang, G. Zhang, P. Hänggi and B. Li, *Rev. Mod. Phys.*, 2012, **84**, 1045-1066.

86. N. Zeng and J. S. Wang, *Phys. Rev. B*, 2008, **78**, 024305.

87. M. Terraneo, M. Peyrard and G. Casati, *Phys. Rev. Lett.*, 2002, **88**, 094302.

88. C. J. Tang, X. X. Yu, G. Li, N. Yang and J. T. Lü, *ES Mater. Manuf.*, 2019, **3**, 16–21.

89. B. Li, J. Lan and L. Wang, *Phys. Rev. Lett.*, 2005, **95**, 104302.

90. B. Hu, L. Yang and Y. Zhang, *Phys. Rev. Lett.*, 2006, **97**, 124302.

91. Y. Dong, C. Diao, Y. Song, H. Chi, D.J. Singh and J. Lin, *Phys. Rev. Appl.*, 2019, **11**, 024043.

92. L. Wang and B. Li, *Phys. World*, 21 (2008) 27.

93. N. Yang, G. Zhang and B. Li, *Appl. Phys. Lett.*, 2008, **93**, 111.

94. N. Yang, G. Zhang and B. Li, *Appl. Phys. Lett.*, 2009, **95**, 033107.

95. J. Hu, X. Ruan and Y. P. Chen, *Nano Lett.*, 2009, **9**, 2730-2735.

96. C. W. Chang, D. Okawa, A. Majumdar, A. Zettl, *Science*, 2006, **314**, 1121.

97. N. Yang, N. Li, L. Wang and B. Li, *Phys. Rev. B*, 2007, **76**, 020301.

98. Y. Wang, S. Chen and X. Ruan, *Appl. Phys. Lett.*, 2012, **100**, 163101.

99. S. Hu, M. An, N. Yang and B. Li, *Small*, 2017, **13**, 1602726.

100. H. Wang, S. Hu, K. Takahashi, X. Zhang and H. Takamatsu, J. Chen, *Nat. Commun.*, 2017, **8**, 15843.

101. Y. Wang, A. Vallabhaneni, J. Hu, B. Qiu, Y. P. Chen and X. Ruan, *Nano Lett.*, 2014, **14**, 592-596.

102. G. Zhang and H. Zhang, *Nanoscale*, 2011, **3**, 4604-4607.

103. Z. Q. Ye and B. Y. Cao, *Nanoscale*, 2017, **9**, 11480-11487.

104. X. Yang, D. Yu, B. Cao and A. C. To, *ACS Appl. Mater. Interfaces*, 2017, **9**, 29-35.

105. T. Zhang and T. Luo, *Small*, 2015, **11**, 4657-4665.

106. H. Ma and Z. Tian, *Nano Lett.*, 2018, **18**, 43-48.

107. B. Y. Cao, Y. W. Li, J. Kong, H. Chen, Y. Xu, K. L. Yung and A. Cai, *Polymer*, 2011, **52**, 1711-1715.

108. S. Li, X. Yu, H. Bao and N. Yang, *J. Phys. Chem. C*, 2018, **122**, 13140-13147.

109. H. Ma and Z. Tian, *Appl. Phys. Lett.*, 2017, **110**, 091903.

110. X. Wei, T. Zhang and T. Luo, *Phys. Chem. Chem. Phys.*, 2016, **18**, 32146-32154.

111. T. Zhang and T. Luo, *J. Phys. Chem. B*, 2016, **120**, 803-812.

112. H. Subramanyan, W. Zhang, J. He, K. Kim, X. Li and J. Liu, *J. Appl. Phys.*, 2019, **125**, 095104.

113. G. H. Kim, D. Lee, A. Shanker, L. Shao, M. S. Kwon, D. Gidley, J. Kim and K. P. Pipe, *Nat. Mater.*, 2015, **14**, 295.

114. Y. Xu, X. Wang, J. Zhou, B. Song, Z. Jiang and E. M. Y. Lee, *Sci. Adv.*, 2018, **4**, eaar3031.

115. P. J. O'Brien, S. Shenogin, J. Liu, P. K. Chow, D. Laurencin, P. H. Mutin, M. Yamaguchi, P. Keblinski and G. Ramanath, *Nat. Mater.*, 2012, **12**, 118.

116. T. Zhang, A. R. Gans-Forrest, E. Lee, X. Zhang, C. Qu, Y. Pang, F. Sun and T. Luo, *ACS Appl. Mater. Interfaces*, 2016, **8**, 33326-33334.

117. Z. Liang and M. Hu, *J. Appl. Phys.*, 2018, **123**, 191101.

118. Y. Zhou, Z. Fan, G. Qin, J. Y. Yang, T. Ouyang and M. Hu, *ACS Omega*, 2018, **3**, 3278-3284.

119. W. Zhang, T.S. Fisher and N. Mingo, Numer. Heat Transfer, Part B, 2007, **51**, 333-349.

120. S. Maruyama, *Adv. Numer. Heat Transfer*, 2000, **2**, 189-226.

121. M. Tuckerman, *Statistical mechanics: theory and molecular simulation*, Oxford university press, 2010.

122. Y. Liu, Y. Cheng, R. Hu and X. Luo, *Phys. Lett. A*, 2019, **383**, 2296-2301.

123. R. J. Hardy, *Phys. Rev.*, 1963, **132**, 168-177.

124. S. Lepri, R. Livi and A. Politi, Thermal conduction in classical low-dimensional lattices, *Phys. Rep.*, 2003, **377**, 1-80.

125. K. Sääskilahti, J. Oksanen, R. P. Linna and J. Tulkki, *Phys. Rev. E*, 2012, **86**, 031107.

126. Y. Chalopin and S. Volz, *Appl. Phys. Lett.*, 2013, **103**, 051602.

127. Z. Fan, L. F. C. Pereira, P. Hirvonen, M. M. Ervasti, K. R. Elder, D. Donadio, T. Ala-Nissila and A. Harju, *Phys. Rev. B*, 2017, **95**, 144309.

128. K. Sääskilahti, J. Oksanen, J. Tulkki and S. Volz, *Phys. Rev. B*, 2014, **90**, 134312.

129. Y. Zhou, X. Zhang and M. Hu, *Phys. Rev. B*, 2015, **92**, 195204.

130. K. Sääskilahti, J. Oksanen, S. Volz and J. Tulkki, *Phys. Rev. B*, 2015, **91**, 115426.

131. Y. Zhou and M. Hu, *Phys. Rev. B*, 2017, **95**, 115313.

132. Z. Fan, P. Hirvonen, L. F. C. Pereira, M. M. Ervasti, K. R. Elder, D. Donadio, A. Harju and T. Ala-Nissila, *Nano Lett.*, 2017, **17**, 5919-5924.

133. Z. Fan, H. Dong, A. Harju and T. Ala-Nissila, *Phys. Rev. B*, 2019, **99**, 064308.

134. R. Kubo, *Rep. Prog. Phys.*, 1966, **29**, 255.

135. M. S. Green, *J. Chem. Phys.*, 1952, **20**, 1281-1295.

136. M. S. Green, *J. Chem. Phys.*, 1954, **22**, 398-413.

137. R. Kubo, *J. Phys. Soc. Jpn.*, 1957, **12**, 570-586.

138. Z. Fan, L. F. C. Pereira, H. Q. Wang, J. C. Zheng, D. Donadio and A. Harju, *Phys. Rev. B*, 2015, **92**, 094301.

139. R. J. Hardy, *J. Chem. Phys.*, 2016, **145**, 204103.

140. H. Dong, Z. Fan, L. Shi, A. Harju and T. Ala-Nissila, *Phys. Rev. B*, 2018, **97**, 094305.

141. J. Liu and R. Yang, *Phys. Rev. B*, 2010, **81**, 174122.

142. L. Zhang, M. Ruesch, X. Zhang, Z. Bai and L. Liu, *RSC Adv.*, 2015, **5**, 87981-87986.

143. H. Meng, X. Yu, H. Feng, Z. Xue and N. Yang, *Int. J. Heat Mass Transfer*, 2019, **137**, 1241-1246.

144. X. Wang, M. Kaviany and B. Huang, *Nanoscale*, 2017, **9**, 18022-18031.

145. H. Ma, E. O'Donnel and Z. Tian, *Nanoscale*, 2018, **10**, 13924-13929.

146. R. Tu, Q. Liao, L. Zeng, Z. Liu and W. Liu, *Appl. Phys. Lett.*, 2017, **110**, 101905.

147. A. Henry, G. Chen, S. J. Plimpton and A. Thompson, *Phys. Rev. B*, 2010, **82**, 144308.

148. T. Luo, K. Esfarjani, J. Shiomi, A. Henry and G. Chen, *J. Appl. Phys.*, 2011, **109**, 074321.

149. M. An, B. Demir, X. Wan, H. Meng, N. Yang and T. R. Walsh, *Adv. Theory Simul.*, 2019, **2**, 1800153.

150. A. B. Robbins and A. J. Minnich, *Appl. Phys. Lett.*, 2015, **107**, 201908.

151. J. He, K. Kim, Y. Wang and J. Liu, *Appl. Phys. Lett.*, 2018, **112**, 051907.

152. H. Ma and Z. Tian, *Appl. Phys. Lett.*, 2015, **107**, 073111.

153. G. Kikugawa, T. G. Desai, P. Keblinski and T. Ohara, *J. Appl. Phys.*, 2013, **114**, 034302.

154. X. Wei and T. Luo, *Phys. Chem. Chem. Phys.*, 2018, **20**, 20534-20539.

155. A. Verma, R. Kumar and A. Parashar, *Phys. Chem. Chem. Phys.*, 2019, **21**, 6229-6237.

156. M. Wang, N. Hu, L. Zhou and C. Yan, *Carbon*, 2015, **85**, 414-421.

157. N. Bhardwaj and S. C. Kundu, *Biotechnol. Adv.*, 2010, **28**, 325-347.

158. J. Ma, Q. Zhang, A. Mayo, Z. Ni, H. Yi, Y. Chen, R. Mu, L. M. Bellan and D. Li, *Nanoscale*, 2015, **7**, 16899-16908.

159. Y. Xu, D. Kraemer, B. Song, Z. Jiang, J. Zhou, J. Loomis, J. Wang, M. Li, H. Ghasemi, X. Huang, X. Li and G. Chen, *Nat. Commun.*, 2019, **10**, 1771.

160. B. Zhu, J. Liu, T. Wang, M. Han, S. Valloppilly, S. Xu and X. Wang, *ACS Omega*, 2017, **2**, 3931-3944.

161. C. Lu, S.W. Chiang, H. Du, J. Li, L. Gan, X. Zhang, X. Chu, Y. Yao, B. Li and F. Kang, *Polymer*, 2017, **115**, 52-59.

162. J. Chen, X. Huang, B. Sun and P. Jiang, *ACS Nano*, 2019, **13**, 337-345.

163. M. K. Smith, T. L. Bougher, K. Kalaitzidou and B. A. Cola, *MRS Adv.*, 2017, **2**, 3619-3626.

164.S. Tanaka, F. Hojo, Y. Takezawa, K. Kanie and A. Muramatsu, *ACS Omega*, 2018, **3**, 3562-3570.

165. M. K. Smith, V. Singh, K. Kalaitzidou and B. A. Cola, *ACS Appl. Mater. Interfaces*, 2016, **8**, 14788-14794.

166. L. Dong, X. Xu and B. Li, *Appl. Phys. Lett.*, 2018, **112**, 221904.

167. J. Hu, Y. Huang, Y. Yao, G. Pan, J. Sun, X. Zeng, R. Sun, J. B. Xu, B. Song and C. P. Wong, *ACS Appl. Mater. Interfaces*, 2017, **9**, 13544-13553.

168. X. Zhang, J. Zhang, L. Xia, C. Li, J. Wang, F. Xu, X. Zhang, H. Wu and S. Guo, *ACS Appl. Mater. Interfaces*, 2017, **9**, 22977-22984.

169. Z. Zhong, M. C. Wingert, J. Strzalka, H. H. Wang, T. Sun, J. Wang, R. Chen and Z. Jiang, *Nanoscale*, 2014, **6**, 8283-8291.

170. Y. Zhang, X. Zhang, L. Yang, Q. Zhang, M. L. Fitzgerald, A. Ueda, Y. Chen, R. Mu, D. Li and L. M. Bellan, *Soft Matter*, 2018, **14**, 9534-9541.

171. A. Pullanchiyodan, K. S. Nair and K. P. Surendran, *ACS Omega*, 2017, **2**, 8825-8835.

172. A. Shanker, C. Li, G. H. Kim, D. Gidley, K.P. Pipe and J. Kim, *Sci. Adv.*, 2017, **3**, e1700342.

173. F. Jiang, S. Cui, N. Song, L. Shi and P. Ding, *ACS Appl. Mater. Interfaces*, 2018, **10**, 16812-16821.

174. S. Waheed, J. M. Cabot, P. Smejkal, S. Farajikhah, S. Sayyar, P. C. Innis, S. Beirne, G. Barnsley, T. W. Lewis, M. C. Breadmore and B. Paull, *ACS Appl. Mater. Interfaces*, 2019, **11**, 4353-4363.

175. X. Chen, M. An, R. Guo, N. Tang, Z. Peng, H. Feng, X. Li, J. Zang and N. Yang, *MRS Adv.*, 2017, **2**, 3651-3656.

176. Y. Li, N. Mehra, T. Ji, X. Yang, L. Mu, J. Gu and J. Zhu, *Nanoscale*, 2018, **10**, 1695-1703.

177. N. Tang, Z. Peng, R. Guo, M. An, X. Chen, X. Li, N. Yang and J. Zang, *Polymers*, 2017, **9**, 688.

178. A. M. Islam, H. Lim, N. H. You, S. Ahn, M. Goh, J. R. Hahn, H. Yeo and S. G. Jang, *ACS Macro Lett.*, 2018, **7**, 1180-1185.

179. X. Xie, D. Li, T. H. Tsai, J. Liu, P. V. Braun and D. G. Cahill, *Macromolecules*, 2016, **49**, 972-978.

180. N. Mehra, Y. Li and J. Zhu, *J. Phys. Chem. C*, 2018, **122**, 10327-10333.

181. L. Mu, J. He, Y. Li, T. Ji, N. Mehra, Y. Shi and J. Zhu, *J. Phys. Chem. C*, 2017, **121**, 14204-14212.

182. C. Monachon, L. Weber and C. Dames, *Annu. Rev. Mater. Res.*, 2016, **46**, 433-463.

183. C. Yuan, M. Huang, Y. Cheng and X. Luo, *Phys. Chem. Chem. Phys.*, 2017, **19**, 7352-7358.

184. S. T. Huxtable, D. G. Cahill, S. Shenogin, L. Xue, R. Ozisik, P. Barone, M. Usrey, M. S. Strano, G. Siddons and M. Shim, *Nat Mater*, 2003, **2**, 731.

185. Z. Lin, Y. Liu, S. Raghavan, K. S. Moon, S. K. Sitaraman and C. P. Wong, *ACS Appl. Mater. Interfaces*, 2013, **5**, 7633-7640.

186. Z. Tian, A. Marconnet and G. Chen, *Appl. Phys. Lett.*, 2015, **106**, 211602.

187. K. Zheng, F. Sun, J. Zhu, Y. Ma, X. Li, D. Tang, F. Wang and X. Wang, *ACS Nano*, 2016, **10**, 7792-7798.

188. J. Liu, S. Ju, Y. Ding and R. Yang, *Appl. Phys. Lett.*, 2014, **104**, 153110.

189. S. A. Putnam, D. G. Cahill, B. J. Ash and L. S. Schadler, *J. Appl. Phys.*, 2003, **94**, 6785-6788.

190. K. Zheng, J. Zhu, Y. M. Ma, D. W. Tang and F. S. Wang, *Chin. Phys. B*, 2014, **23**, 107307.

191. K. Zheng, F. Sun, X. Tian, J. Zhu, Y. Ma, D. Tang and F. Wang, *ACS Appl. Mater. Interfaces*, 2015, **7**, 23644-23649.